



# Topology optimization with local stress constraints: a stress aggregation-free approach

Fernando V. Senhora<sup>1,2</sup> · Oliver Giraldo-Londoño<sup>1</sup> · Ivan F. M. Menezes<sup>2</sup> · Glaucio H. Paulino<sup>1</sup>

Received: 23 July 2018 / Revised: 27 February 2020 / Accepted: 9 March 2020 / Published online: 20 August 2020  
© Springer-Verlag GmbH Germany, part of Springer Nature 2020

## Abstract

This paper presents a consistent topology optimization formulation for mass minimization with local stress constraints by means of the augmented Lagrangian method. To solve problems with a large number of constraints in an effective way, we modify both the penalty and objective function terms of the augmented Lagrangian function. The modification of the penalty term leads to consistent solutions under mesh refinement and that of the objective function term drives the mass minimization towards black and white solutions. In addition, we introduce a piecewise vanishing constraint, which leads to results that outperform those obtained using relaxed stress constraints. Although maintaining the local nature of stress requires a large number of stress constraints, the formulation presented here requires only one adjoint vector, which results in an efficient sensitivity evaluation. Several 2D and 3D topology optimization problems, each with a large number of local stress constraints, are provided.

**Keywords** Consistent topology optimization · Augmented Lagrangian · Stress constraints · Stress relaxation · von Mises stress · Aggregation-free

## 1 Introduction

Cauchy was a visionary mathematician, physicist, and engineer who made pioneering contributions to several fields of knowledge, including continuum mechanics and elasticity (Bell 1986). Inspired by his work on continuum mechanics, we introduce a consistent stress-constrained topology optimization formulation that treats stress as a local quantity both in the solution of the boundary value problem and in the optimization phase. By treating stresses locally, we follow its definition as a fundamental quantity obtained by means of a limiting process known as Cauchy's tetrahedron

argument (Cauchy 1827; Love 1892; Timoshenko and Goodier 1951; Malvern 1969; Gurtin 1981). The argument states that the stress vector acting on a small area  $da$  oriented perpendicular to its normal vector  $\mathbf{n}$  and located at a point in a continuous medium depends on the infinitesimal internal force vector  $d\mathbf{f}(\mathbf{n})$  acting on that surface, and it is defined as (Cauchy 1827):

$$\boldsymbol{\sigma} \cdot \mathbf{n} = \lim_{\Delta a \rightarrow 0} \frac{\Delta \mathbf{f}(\mathbf{n})}{\Delta a}, \quad (1)$$

where  $\boldsymbol{\sigma}$  is the stress tensor. In this paper, we treat stress consistently, i.e., as a local quantity.

The solution of a consistent topology optimization problem with local stress constraints comes with its own set of challenges. First, as stress is a local quantity that must be satisfied pointwise, one needs to impose a large number of constraints, leading to a prohibitive computational cost. Second, as the optimal solution of a stress-constrained problem generally lies on a degenerated region with dimension smaller than that of the design space, one needs a gradient-based optimization technique able to reach inside those regions. The formulation presented here attempts to address these challenges, such that we can efficiently find optimized structures that meet material strength limits at all evaluation points under consideration.

---

Responsible Editor: Kurt Maute

---

Dedicated to the memory of Augustin-Louis Cauchy (August 21, 1789 – May 23, 1857)

---

✉ Glaucio H. Paulino  
paulino@gatech.edu

<sup>1</sup> School of Civil and Environmental Engineering, Georgia Institute of Technology, 790 Atlantic Drive, Atlanta, GA 30332, USA

<sup>2</sup> Pontifical Catholic University of Rio de Janeiro (PUC-Rio), Rua Marques de Sao Vicente, 225, Rio de Janeiro, R.J. 22453, Brazil

In order to solve the consistent topology optimization problem with *local stress constraints*, we employ an augmented Lagrangian (AL) approach, which yields designs that do not violate the stress limit at any evaluation point of the discretized domain. While preserving the local nature of stress, we solve the consistent topology optimization problem efficiently using gradient-based optimization algorithms. The efficiency results from the sensitivity evaluation, which requires the computation of only one adjoint vector (i.e., one additional linear solution) at each optimization step. To reach inside the degenerated region of the design space in which the optimal solution generally lies, we use a variation of the traditional vanishing constraint (Cheng and Jiang 1992), which we define as a *piecewise vanishing constraint*. The new constraint definition leads to feasible solutions and is proven to work well within our AL-based framework.

The remainder of this paper is organized as follows. Section 2 extends the motivation for this work and discusses several studies in stress-constrained topology optimization. Section 3 details relevant issues regarding the problem of singular optima and their implications in stress-constrained topology optimization. We discuss some theoretical considerations of the AL method in Section 4 and present our AL-based consistent topology optimization framework in Section 5. The sensitivity analysis is presented in detail in Section 6. Implementation details of our AL-based formulation are provided in Section 7. Then, we present several 2D and 3D examples in Section 8, followed by an analysis of the computational efficiency of the formulation in Section 9. We conclude the paper in Section 10 with some remarks and our own perspective on the stress constraint problem. Afterward, we provide several appendices. Appendix A provides details of the AL method to handle inequality constraints. Appendix B provides a comparison between the apparent “local” von Mises stress (Duysinx and Bendsøe 1998a) and the stress measure adopted in this study. In Appendix C, the optimization results obtained using our stress constraint definition are compared against those obtained using the  $\varepsilon$ -relaxed constraint by Cheng and Guo (1997). Appendices D and E address the modifications introduced to the AL function in the optimization results for an  $L$ -bracket. Appendices F and G present additional numerical results related to the effect of restarting the parameters of the AL function as well as the effects of varying the stress limit of the solid material, respectively. Finally, Appendix H contains the nomenclature used in the present study.

## 2 Related work

The overall goal of topology optimization is to find a material distribution in a given design domain such that an objective

function is minimized (Bendsøe 1995). Since the pioneering work by Bendsøe and Kikuchi (1988), most developments in topology optimization have concentrated on compliance minimization problems, which aim to find the stiffest structure for a given volume constraint. Because no limits on material strength are imposed, structures designed for minimum compliance do not necessarily withstand the applied loads, thus making some of these designs unfeasible for practical applications involving strength-related considerations. Therefore, from a structural integrity standpoint, a more appropriate topology optimization formulation should aim to find the lightest structure that resists the applied loads without exceeding the material strength.

To guarantee that the loads do not exceed the material strength, the formulation must consider stress constraints. However, stress is local by nature, which in the context of topology optimization, implies that a large number of stress evaluation points, and consequently a large number of stress constraints, are necessary to guarantee the structural integrity of the final design. Due to the large number of stress constraints, topology optimization problems with local stress constraints demand high computational resources both for the sensitivity evaluation and for the optimization problem, which makes the direct problem intractable (Duysinx and Bendsøe 1998a).

To reduce the computational cost, most researchers have used aggregation techniques to transform the local stress constraints into a single global constraint (e.g., see Yang and Chen 1996; Duysinx and Sigmund 1998b; Lee et al. 2012; Xia et al. 2012; Lian et al. 2017; Sharma and Maute 2018). The main idea of these techniques is to construct one global stress measure that approximates the maximum stress in the design domain. Because the maximum function is not differentiable, and thus, not suitable for gradient-based optimization algorithms, smooth approximations of the maximum function have been used instead. Among the most popular functions used in this context are the Kreisselmeier–Steinhauser (KS) (Kreisselmeier and Steinhauser 1979) and the  $p$ -norm (Park 1995) functions. Yang and Chen (1996) used these two aggregation functions to design structures subjected to stress constraints and found that the aggregation functions may become unstable when the numerical parameter  $p$  is large. Duysinx and Sigmund (1998b) tested two global stress measures, one based on the  $p$ -norm function and the other on the  $p$ -mean function. Both aggregation functions were used in conjunction with a relaxation technique to solve stress-constrained topology optimization problems. Their study confirmed that, although  $p$  should be taken as large as possible, the optimization problem becomes ill-conditioned and unstable as  $p$  increases.

The use of a global stress measure reduces the computational cost at the price of losing control over the

local behavior of stress (Duysinx and Sigmund 1998b; Le et al. 2010). The ability of aggregation functions to represent the local stress constraints depends on the number of constraints, and it can rapidly deteriorate as this number increases. To circumvent this issue, some researchers have used *clustering techniques*, in which the design domain is first divided in several sub-regions, each called a cluster, and then an aggregation function (e.g., the  $p$ -norm) is used to approximate the maximum stress value in each cluster (e.g., see Le et al. 2010; Holmberg et al. 2013; Paris et al. 2010). However, this strategy raises a couple of questions:

1. How many clusters should be used?
2. How should the clusters be defined? (i.e., how many elements should be included in each cluster and what type of clustering function should be used?).

The resulting topologies obtained using the aforementioned clustering techniques strongly depend on the number of clusters and on the way the clusters are defined. Although it is expected that increasing the number of clusters leads to increasing control over the local stress, there is no clear relation between the number of clusters and the quality of the optimized results (Le et al. 2010).

In addition to aggregation techniques, *active set* methods have been used to reduce the computational cost of topology optimization problems with local stress constraints (Duysinx and Bendsoe 1998a, b; Guo et al. 2011; Bruggi and Duysinx 2012). In the active set method, only active stress constraints, i.e., constraints that are violated or close to being so, are considered in the sensitivity evaluation, thus reducing the computational cost considerably. However, this method may not be suitable for large-scale topology optimization problems with local stress constraints because, as the mesh is refined, the number of active constraints increases, and as the optimization progresses, the number of elements reaching the stress limit increases.

A different method that has been used to reduce the computational cost of stress constraint topology optimization problems is based on the concept of *topological derivatives* (Amstutz and Novotny 2010). In this approach, the local stress constraints are used to define a class of von Mises stress penalty functional, whose topological derivative is employed as the descent direction in a topology optimization algorithm.

An attractive approach to efficiently solve topology optimization problems with local stress constraints is the AL method (Bertsekas 1996, 1999). This method directly deals with local stress constraints by adding them to the objective function in the form of a penalty term that is updated at each optimization step. As a result, the sensitivity information in AL-based methods can be computed efficiently via the adjoint method. The sensitivity analysis can be conducted

efficiently because, independently of the number of stress constraints, one only needs to compute a single adjoint vector at every optimization step. Pereira et al. (2004) used the AL method in the context of density-based topology optimization using relaxed local stress constraints (Cheng and Guo 1997). Although promising, the strategy by Pereira et al. (2004) appears to have difficulties finding 0/1 solutions at the end of the optimization steps. The AL method was also used by Emmendoerfer and Fancello (2014, 2016) and by James et al. (2012) in the context of the level-set method. In the approach by Emmendoerfer and Fancello (2014, 2016), the AL method is used to treat the von Mises stresses as local quantities, and in the approach by James et al. (2012), the AL method is used to enforce volume constraints, while the local von Mises stress values are aggregated using a  $p$ -norm aggregation function. The approach by Emmendoerfer and Fancello (2014, 2016) produces structures with clear boundaries that satisfy the stress constraints locally, but the algorithmic parameters required for the evolution of the level set may change from one problem to another, which undermines the robustness of their approach. Moreover, da Silva et al. (2019) used the AL method for stress-constrained topology optimization considering manufacturing uncertainties via eroded, intermediate, and dilated projections (Sigmund 2009).

In addition to the locality of stress constraints, another challenge in stress-constrained topology optimization problems that has received a lot of attention is related to the phenomenon of singular optima. This phenomenon was first reported by Sved and Ginos (1968) when dealing with stress-constrained truss optimization. In their paper, Sved and Ginos (1968) studied a three-bar truss subjected to stress constraints, and found that the global optimum could only be obtained if one of the bars was removed from the topology. This implies that the solution lies at a singular point in the design space (i.e., in a degenerated region with a smaller dimension than that of the solution space), and thus, these optima points do not satisfy standard constraint qualification (Achtziger and Kanzow 2008). Achtziger and Kanzow (2008) classified this type of optimization problem as a mathematical program with vanishing constraints (MPVCs), and proposed a modified constraint qualification that holds under certain assumptions. Hoheisel and Kanzow (2008) elaborated on Achtziger and Kanzow's work and proposed several tailored versions of standard constraint qualification for MPVCs. The phenomenon of singular optima was extensively studied by other researchers (Kirsch and Taye 1986, 1989, 1990; Cheng and Jiang 1992). A thorough historical review on the subject can be found in a study by Rozvany (2001).

The issue of singular optima has been alleviated by means of relaxation techniques such as the  $\varepsilon$ -relaxation

(Cheng and Guo 1997). This relaxation technique was developed in the context of truss optimization, such that the singular optima were removed by allowing higher stresses in elements of smaller area. Duysinx and Sigmund (1998b) modified the  $\varepsilon$ -relaxed constraint by Cheng and Guo (1997) for use in the context of density-based topology optimization. As an alternative methodology to the  $\varepsilon$ -relaxation approach, Bruggi (2008) proposed the so-called qp-relaxation technique. In the qp-relaxation, a suitable penalty exponent is used to interpolate the stress limit, in a similar way as stiffness is interpolated in the SIMP method (Bendsoe and Sigmund 1989, 1999). Bruggi (2008) showed that the qp-relaxation is similar to an adaptive  $\varepsilon$ -relaxation, in which  $\varepsilon$  is a function of the element density. Achtziger et al. (2013) proposed a smooth-regularization approach that, in some way, resembles existing relaxation techniques in the sense that it is controlled by a numerical factor,  $t$ , such that as  $t$  tends to zero the original problem is obtained. Achtziger et al. (2013) proved that this version of the problem satisfies standard constraint qualification and also provides a study on the effects of  $t$  on the optima points of the problem. The issue of singular optima as well as relaxation techniques are a key aspect in the development of the current optimization framework, and thus, we provide a more detailed explanation in the next section.

As a natural way to handle both the locality and the singular optima problems, Verbart et al. (2016) proposed a damage-like approach for stress-constrained topology optimization. In their formulation, any material point in which the stress limit has been exceeded is considered as damaged, and consequently contributes less to the overall stiffness of the structure. With stiffness as a performance measure, their method indirectly favors designs with the least amount of material damaged due to stress violation. Although efficient, the method by Verbart et al. (2016) may lead to structures that violate the stress limit.

Most of the methods discussed so far have numerical parameters, which tend to be both problem- and mesh-dependent. Therefore, each new problem requires an empirical adjustment step, which is undesirable for practical purposes. In order to reduce the number of parameters to be calibrated, Verbart et al. (2017) presented an approach that aims to unify aggregation and relaxation techniques. They showed that using a lower bound aggregation function also relaxes the feasible domain, removing the need for relaxation in stress-constrained topology optimization. However, as in traditional constraint aggregation approaches, the choice of the aggregation parameter is both problem- and mesh-dependent.

Overall, stress-constrained topology optimization is still an open problem that lacks an efficient and robust

methodology that is suitable to solve large-scale problems considering local stress constraints. We propose an AL-based formulation that treats stresses as local quantities, leading to designs that do not exceed stress limits anywhere in the design domain. With two new parameters that are used to adapt the traditional AL function, the formulation introduced in this study is stable for various mesh sizes and can efficiently handle problems with a considerably large number of stress constraints. These two modifications are defined in terms of a default set of parameters (which need not be modified from one problem to another) and are used to solve various topology optimization problems whose number of stress constraints ranges between a few thousands to over one million. The method is shown to be robust by providing consistent solutions to stress-constrained topology optimization problems in both 2D and 3D.

### 3 A brief discussion on singular optima

This section elaborates on the singularity phenomenon discussed previously. To this purpose, we introduce a simple mass minimization problem in the context of density-based topology optimization, which is analogous to the three-bar truss problem studied by Kirsch (1990). This new problem, which has not been discussed elsewhere, demonstrates the singularity phenomenon in the context of density-based topology optimization. Particularly, this problem shows that solutions of density-based topology optimization problems with stress constraints may lie in degenerated regions that are disconnected from the rest of the solution space. Finally, we discuss some of the relaxation strategies that have been used to alleviate the problems associated with the singularity phenomenon.

#### 3.1 Diagonal square problem

In this section, we suggest a simple example, which we have named the *diagonal square problem*, to study the singularity phenomenon in the context of density-based optimization. This new example resembles the benchmark three-bar truss problem (Kirsch 1990; Rozvany and Birker 1994; Cheng and Guo 1997), which introduces the singularity phenomenon in the context of ground structures. Figure 1a illustrates the geometry, boundary conditions, and loading for the suggested example. The model consists of a square of side  $L = 2$  (consistent units are used) that is discretized using a  $2 \times 2$  mesh. Two of the elements have a fixed density equal to 1, and the other two have densities controlled by  $\rho_1$  and  $\rho_2$  (the design variables). The objective is to minimize

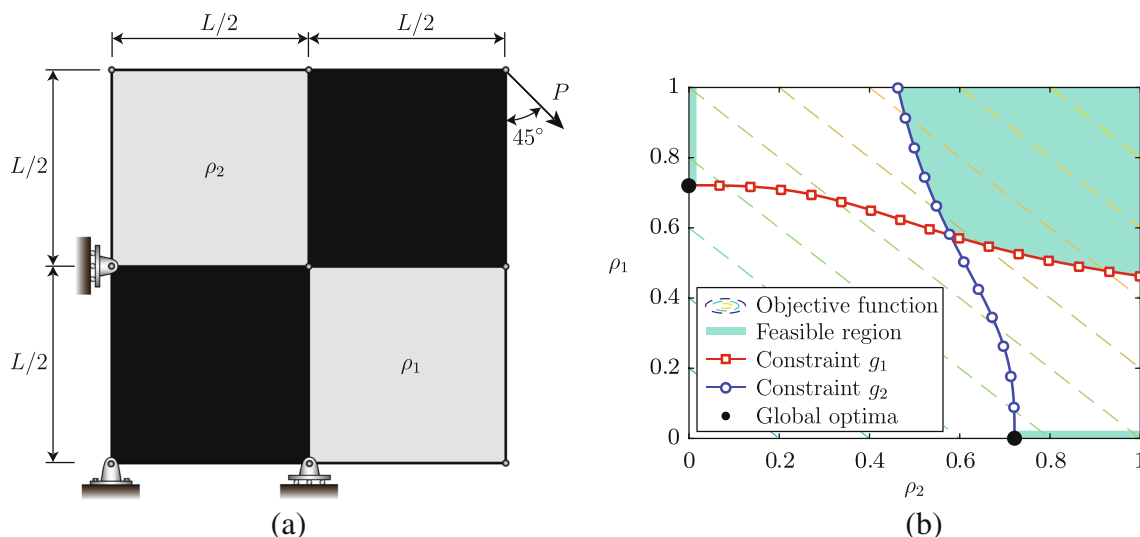


**Fig. 1** Diagonal square problem: **a** geometry, boundary conditions, and loading; and **b** feasible design space. Notice that the global optima are located in degenerate regions that are disconnected from the remainder of the feasible region

the volume subjected to constraints on the von Mises stress. The optimization statement is formulated as follows:

$$\begin{aligned}
 \min_{(\rho_1, \rho_2)} \quad & m(\rho_1, \rho_2) = \rho_1 + \rho_2 \\
 \text{s.t.} \quad & g_1 = \frac{\sigma_1^v}{\sigma_{\text{lim}}} - 1 \leq 0, \quad \rho_1 > 0 \\
 & g_2 = \frac{\sigma_2^v}{\sigma_{\text{lim}}} - 1 \leq 0, \quad \rho_2 > 0 \\
 & 0 \leq \rho_i \leq 1, \quad i = 1, 2
 \end{aligned} \tag{2}$$

with:  $\mathbf{K}(\rho_1, \rho_2)\mathbf{u} = \mathbf{f}$ ,

where  $\sigma_1^v$  and  $\sigma_2^v$  are the apparent “local” von Mises stresses of the elements associated with design variables  $\rho_1$  and  $\rho_2$ , respectively (Duysinx and Bendsoe 1998a, b), and are evaluated at the centroid of each element. The stress limit  $\sigma_{\text{lim}} = 1$  is the maximum von Mises stress for the solid material. The stiffness matrix,  $\mathbf{K}$ , is obtained through a typical assembly process, such that the element stiffness matrices are obtained as  $\mathbf{k}_e = [\epsilon + (1 - \epsilon)\rho_e^p]\mathbf{k}_0$ , in which  $\mathbf{k}_0$  is the stiffness matrix for solid material,  $p = 3$  is the SIMP exponent, and  $\epsilon = 1 \times 10^{-6}$  is the Ersatz stiffness. The Young’s modulus and Poisson’s ratio for the solid material are  $E_0 = 1$  and  $\nu = 0.3$ , respectively. The applied load is  $\mathbf{P} = [0.1, -0.1]^T$ , such that the value of  $P$  in Fig. 1a is  $P = \|\mathbf{P}\| = \sqrt{2}/10$ .

The objective function and the feasible design space are depicted in Fig. 1b. The solution space of the current problem contains degenerated feasible regions with dimension smaller than that of the design space. The degenerated regions of the current problem are disconnected from the rest of the feasible design domain, which imposes additional challenges to the numerical solution of the optimization statement (2). To obtain the degenerated regions of the feasible design space, one must recall that

stress constraints  $g_1$  and  $g_2$ , given in (2), are only valid if  $\rho_1 > 0$  and  $\rho_2 > 0$ , respectively. Consequently, if  $\rho_1 = 0$ , constraint  $g_1$  has no meaning and if  $\rho_2 = 0$ , constraint  $g_2$  has no meaning, leading to the degenerated regions on the  $\rho_2$  and  $\rho_1$  axes of Fig. 1b, respectively.

### 3.2 On strategies for finding singular optima

Obtaining the global optima for the type of problems discussed previously is challenging due to degenerated regions of the feasible design space (e.g., see Fig. 1b). In order to obtain the global optima for the three-bar truss problem, Cheng and Jiang (1992) proposed to replace the stress constraints with internal force constraints. Although internal force constraints are not consistent with density-based stress-constrained topology optimization, an analogue of the internal force constraint can still be used in this context. These alternative constraints, which are referred to as vanishing constraints,<sup>1</sup> are written as follows:

$$\tilde{g}_1 = \rho_1 g_1 \text{ and } \tilde{g}_2 = \rho_2 g_2. \tag{3}$$

This simple modification removes the discontinuity of the constraints when any of the densities vanish.

Although the vanishing constraints remove the discontinuity of stress constraints  $g_i$  when  $\rho_i = 0$ , the feasible region remains unchanged (i.e., the global optimum still belongs to a region of smaller dimension than that of the rest of the design space). As a result, traditional gradient-based optimization algorithms may have difficulties in finding optimal points. To overcome this difficulty, Cheng and Guo (1997) proposed the so-called  $\epsilon$ -relaxation approach. This

<sup>1</sup>A variation of the vanishing constraints is used in the present study to solve stress-constrained topology optimization problems.

approach was proposed for truss optimization, such that the stress constraints are written as internal force constraints that are set to be smaller than a small positive quantity,  $\varepsilon$ , which controls the extent of the relaxation. The  $\varepsilon$ -relaxed approach has also been used to solve density-based stress-constrained topology optimization problems, in which the constraint takes the form:

$$g_\varepsilon(\rho) = \frac{\sigma^v}{\sigma_{\text{lim}}} - 1 - \frac{\varepsilon}{\rho} \leq 0, \tag{4}$$

where  $\sigma^v$  is the apparent ‘‘local’’ von Mises stress (Duysinx and Bendsoe 1998a, b), computed using the elasticity matrix of the solid material (i.e., using the Cauchy stress tensor computed as  $\sigma = \mathbf{D}_0\epsilon$ , in which  $\mathbf{D}_0$  is the elasticity matrix of the solid material and  $\epsilon$  is the infinitesimal strain tensor expressed in Voight notation), and  $\rho$  is the density of the element associated with constraint  $g_\varepsilon$ . This method relaxes the feasible design space, increasing the dimensionality of the degenerated regions. In addition to modifying the stress constraints according to (4), the  $\varepsilon$ -relaxation approach requires a modification to the variable lower bounds, such that  $\rho_i \geq \varepsilon^2$ . The modification to the variable lower bound is a condition imposed to guarantee convergence of the  $\varepsilon$ -relaxation approach<sup>2</sup> (Cheng and Guo 1997; Petersson 2001).

To solve stress-constrained topology optimization problems using the  $\varepsilon$ -relaxed approach, it has been suggested to start with a relatively large value of  $\varepsilon$  until a solution is obtained and then solve the optimization problem again using a smaller value of  $\varepsilon$  and the previous solution as an initial guess. The procedure is repeated until a sufficiently small value of  $\varepsilon$  is reached. According to Cheng and Guo (1997), the sequence of solutions for decreasing values of  $\varepsilon$  leads to a global optimum of the stress-constrained optimization problem. However, Stolpe and Svanberg (2001) studied the trajectories followed by the sequence of solutions and found that the sequence of solutions to the  $\varepsilon$ -relaxed problem may not lead to a global optimum of the original problem. In fact, they showed that the trajectories followed by the sequence of solutions may be non-smooth and even discontinuous.

An alternative to the  $\varepsilon$ -relaxed approach to deal with the singularity phenomenon in stress-constrained topology optimization is the qp-relaxation (Bruggi 2008). The idea of the qp-relaxation is to interpolate the stress limit of the material using the SIMP approach, with a penalty exponent  $q < p$ , where  $p$  is the penalty exponent used to interpolate

the stiffness of the material. This leads to stress constraints written as

$$g_{\text{qp}}(\rho) = \rho^{p-q} \frac{\sigma^v}{\sigma_{\text{lim}}} - 1 \leq 0. \tag{5}$$

The choice of  $q < p$  eliminates the discontinuity of the local stresses when the density becomes zero. In the study by Bruggi (2008), it is shown that the qp-relaxation can be interpreted as an adaptive  $\varepsilon$ -relaxation in which  $\varepsilon$  is a function of the density  $\rho$ . Bruggi (2008) suggested a similar continuation scheme as that used in the  $\varepsilon$ -relaxed approach.

To illustrate the effect of the relaxation techniques on the stress constraints, let us recall the optimization statement (2) for the diagonal square problem. For the sake of simplicity, we only show the effects of the relaxation using the  $\varepsilon$ -relaxed approach because the qp-relaxation behaves in a similar way. The original constraints,  $g_1$  and  $g_2$ , and the relaxed constraints,  $g_\varepsilon^{(1)}$  and  $g_\varepsilon^{(2)}$  (obtained using (4)), are shown in Fig. 2 for  $\varepsilon = 0.3$ .

Because approaches such as the  $\varepsilon$ -relaxation or the qp-relaxation relax the design space, the solution of the relaxed problem might lead to a material distribution that is unfeasible with respect to the original constraints. That is because satisfaction of the relaxed constraints does not imply satisfaction of the original constraints—an issue that may become severe for large-scale optimization problems. On the other hand, if the relaxation is too moderate (e.g., if  $\varepsilon \rightarrow 0$  for the  $\varepsilon$ -relaxation technique), the optimal points might not be reachable through standard optimization techniques.

### 4 Augmented Lagrangian

The AL method is a numerical technique used to solve constrained optimization problems. This technique

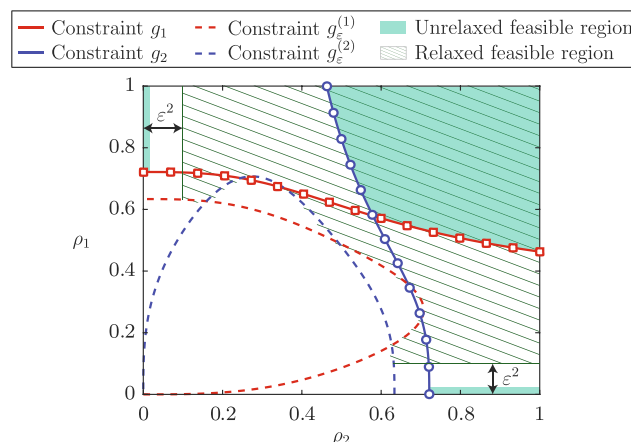


Fig. 2 Relaxed constraints for the diagonal square problem. Constraints  $g_\varepsilon^{(1)}$  and  $g_\varepsilon^{(2)}$  correspond to the  $\varepsilon$ -relaxed constraints of  $g_1$  and  $g_2$ , respectively, using  $\varepsilon = 0.3$

<sup>2</sup>According to Cheng and Guo (1997), the restriction on the variable lower bound to be  $\varepsilon^2$  is not necessary. They demonstrated that, in order to guarantee convergence, the lower bound on the design variables has to be a higher order term smaller than  $\varepsilon$  as  $\varepsilon \rightarrow 0$ .

is fundamentally different from constraint aggregation techniques, in which, according to Ermoliev et al. (1997), the original problem is replaced by another problem or a sequence of problems, such that the local constraints are replaced by a surrogate inequality. The AL method, which is an improvement to the quadratic penalty method, has a well-established mathematical background (e.g., see Bertsekas 1996, 1999; Nocedal and Wright 2006), which motivates our choice. In the AL method, the solution of a constrained optimization problem is achieved by solving a series of unconstrained problems that are expected to converge to the solution of the original constrained optimization problem. For instance, suppose that we aim to solve the optimization problem

$$\begin{aligned} \min_{\mathbf{z} \in \mathbb{R}^n} \quad & f(\mathbf{z}) \\ \text{s.t.} \quad & h_j(\mathbf{z}) = 0 \quad \forall j = 1, \dots, N_c, \end{aligned} \tag{6}$$

where  $\mathbf{z}$  is the vector of design variables,  $f(\mathbf{z})$  is the objective function,  $h_j(\mathbf{z})$  are the equality constraints, and  $N_c$  is the number of constraints. The unconstrained optimization problem that is solved at the  $k$ th step of the AL method is as follows:

$$\min_{\mathbf{z} \in \mathbb{R}^n} \quad J^{(k)}(\mathbf{z}) = f(\mathbf{z}) + \sum_{j=1}^{N_c} \left[ \lambda_j^{(k)} h_j(\mathbf{z}) + \frac{\mu^{(k)}}{2} h_j(\mathbf{z})^2 \right], \tag{7}$$

where  $\lambda_j^{(k)}$  is an estimate of the Lagrange multiplier of  $h_j(\mathbf{z})$  and  $\mu^{(k)}$  is a penalty coefficient similar to that used in the quadratic penalty method. Both  $\lambda_j^{(k)}$  and  $\mu^{(k)}$  are updated at every step  $k$ . The AL function,  $J^{(k)}(\mathbf{z})$ , is similar to the Lagrangian of the constrained problem (6), but differs from it by the terms  $\frac{1}{2} \mu^{(k)} h_j(\mathbf{z})^2$ . The presence of the terms  $\lambda_j^{(k)}$  in the AL function reduces the possibility of ill-conditioning associated with quadratic penalty methods (Nocedal and Wright 2006).

The solution  $\mathbf{z}^{(k)}$  of the approximate sub-problem (7) tends to converge to the solution  $\mathbf{z}^*$  of the original problem (6) as  $k \rightarrow \infty$ , given that the original problem satisfies some regularity conditions (Nocedal and Wright 2006). Particularly, Bertsekas (1996) proved that if both the objective function and the constraints are continuous, the original problem has an optimum, and every sub-problem has an optimum, then the sequence of optima points of the sub-problems converge to an optimum point of the original problem.<sup>3</sup> Assuming that problem (7) is well-behaved, the

<sup>3</sup>However, the stress-constrained problem is not well-behaved because, given the degenerate nature of the constraints, the Lagrange multiplier set associated with a stationary point is unbounded. For optimization problems of this type, Izmailov et al. (2012) and Andreani et al. (2012) showed that the AL method exhibits global convergence properties, which suggests that this method is a viable alternative to solve stress-constrained topology optimization problems.

first-order optimality condition states that

$$\begin{aligned} \nabla J^{(k)}(\mathbf{z}^{(k)}) &= \nabla f(\mathbf{z}^{(k)}) \\ &+ \sum_{j=1}^{N_c} \left[ \lambda_j^{(k)} + \mu^{(k)} h_j(\mathbf{z}^{(k)}) \right] \nabla h_j(\mathbf{z}^{(k)}) = \mathbf{0}. \end{aligned} \tag{8}$$

Comparing (8) with the KKT optimality conditions for problem (6) implies that

$$\lambda_j^* \nabla h_j(\mathbf{z}^*) \approx \left[ \lambda_j^{(k)} + \mu^{(k)} h_j(\mathbf{z}^{(k)}) \right] \nabla h_j(\mathbf{z}^{(k)}), \tag{9}$$

from which we obtain the following:

$$\lambda_j^* \approx \lambda_j^{(k)} + \mu^{(k)} h_j(\mathbf{z}^{(k)}) \quad \text{or} \quad h_j(\mathbf{z}^{(k)}) \approx \frac{\lambda_j^* - \lambda_j^{(k)}}{\mu^{(k)}}. \tag{10}$$

Equation (10) provides a means for updating the Lagrange multiplier estimators,  $\lambda_j^{(k)}$ , at every step  $k$ , as follows:

$$\lambda_j^{(k+1)} = \lambda_j^{(k)} + \mu^{(k)} h_j(\mathbf{z}^{(k)}), \quad \forall j = 1, \dots, N_c. \tag{11}$$

From the second expression of (10), it is observed that  $h_j(\mathbf{z}^{(k)})$  is proportional to  $\lambda_j^* - \lambda_j^{(k)}$  and inversely proportional to  $\mu^{(k)}$ . Thus, a good estimation of the Lagrange multipliers and a large value of  $\mu^{(k)}$  improve the convergence of the AL method to a feasible solution (i.e.,  $h_j(\mathbf{z}) = 0$ ). In theory, when  $\lambda^{(k)}$  is a good estimate of the actual Lagrange multiplier vector, one can obtain a good estimate of  $\mathbf{z}^*$  by solving the approximate problem (7) without requiring  $\mu^{(k)}$  to be considerably large. Unlike penalty methods in which  $\mu^{(k)} \rightarrow \infty$  as  $k \rightarrow \infty$ , the fact that  $\mu^{(k)}$  needs not become too large in AL methods greatly improves their conditioning (Nocedal and Wright 2006). A proper value for  $\mu^{(1)}$  needs to be chosen carefully because a relatively high initial value for this parameter may lead to ill-conditioning of the optimization problem (Bertsekas 1999, p. 123). The usual recommendation found in the literature (e.g., see Bertsekas 1996, 1999; Nocedal and Wright 2006) is to start with a moderate value of  $\mu^{(1)}$  and gradually increase it according to the following:

$$\mu^{(k+1)} = \alpha \mu^{(k)}, \tag{12}$$

where  $\alpha > 1$  is a constant. The value of  $\alpha$  may also be problem dependent and may require empirical adjustment. To solve optimization problems using the AL method, one needs to solve the unconstrained optimization statement (7) at each step  $k$  and update both Lagrange multipliers  $\lambda_j^{(k)}$  and penalty term  $\mu^{(k)}$ , using (11) and (12), respectively. The procedure is repeated until some convergence criterion is satisfied. The AL method presented here is designed for equality constraints, and extended for inequality constraints in Appendix A.

## 5 Consistent stress-constrained topology optimization formulation

This section presents a framework for the consistent solution of stress-constrained topology optimization problems based on the AL method introduced previously. The optimization statement that we solve in the present study is as follows:

$$\begin{aligned} \min_{\mathbf{z}} \quad & m(\mathbf{z}) = \sum_{e=1}^{N_e} \tilde{\rho}_e v_e \\ \text{s.t.} \quad & g_j(\mathbf{z}) \leq 0, \quad j = 1, \dots, N_c \\ & 0 \leq z_e \leq 1, \quad e = 1, \dots, N_e \\ \text{with:} \quad & \mathbf{K}(\mathbf{z})\mathbf{u} = \mathbf{f}, \end{aligned} \quad (13)$$

where  $m(\mathbf{z})$  is the mass (volume) of the structure,  $\mathbf{z}$  is the vector of design variables,  $\tilde{\rho}_e$  is the volume fraction of element  $e$  defined using a smooth Heaviside projection (Guest et al. 2004),  $\rho(\mathbf{z}) = \mathbf{P}\mathbf{z}$  is the vector of filtered densities,  $\mathbf{P}$  is the filter matrix,  $v_e$  is the area (for 2D problems) or volume (for 3D problems) of element  $e$ ,  $g_j(\mathbf{z})$  is the  $j$ th stress constraint,  $N_c$  is the number of stress constraints,  $N_e$  is the number of elements in the finite element mesh, and  $\mathbf{K}(\mathbf{z})\mathbf{u} = \mathbf{f}$  is the typical linear elastic equilibrium equation,<sup>4</sup> which is solved using the finite element method. The stiffness matrix is computed through a typical assembly process as follows:

$$\mathbf{K}(\mathbf{z}) = \mathbb{A} \sum_{e=1}^{N_e} \mathbf{k}_e, \quad \text{with } \mathbf{k}_e = [\epsilon + (1 - \epsilon)\rho_e^p] \mathbf{k}_0, \quad (14)$$

where  $\mathbf{k}_e$  are the element stiffness matrices, in which  $\epsilon$  is the Ersatz parameter,  $p$  is the SIMP penalization factor, and  $\mathbf{k}_0$  is the stiffness matrix for a solid element.

In this study, we have adopted the filter used by Zegard and Paulino (2016), which we have denoted as *polynomial filter*. For this type of filter, the filter matrix,  $\mathbf{P}$ , is computed as:

$$P_{ij} = \frac{w_{ij}v_j}{\sum_{k=1}^{N_e} w_{ik}v_k}, \quad \text{with } w_{ij} = \max \left[ 0, 1 - \frac{\|\mathbf{x}_i - \mathbf{x}_j\|_2}{r} \right]^s, \quad (15)$$

where  $r$  is the filter radius and  $\|\mathbf{x}_i - \mathbf{x}_j\|_2$  represents the distance between the centroids,  $\mathbf{x}_i$  and  $\mathbf{x}_j$ , of elements  $i$  and  $j$ , respectively. The order of the filter is defined by the filter exponent,  $s$ . Note that, when  $s = 1$ , the polynomial filter reduces to the traditional linear filter (Bourdin 2001).

In a traditional mass minimization topology optimization problem with stress constraints, the mass is usually computed as  $m(\mathbf{z}) = \sum_{e=1}^{N_e} \rho_e(\mathbf{z})v_e$ . Several researchers

<sup>4</sup>Notice the modular structure developed for the stress-constrained topology optimization problem. Due to this feature, different constitutive behaviors can be incorporated in the present computational mechanics framework.

have used different mass functions that penalize intermediate densities to facilitate obtaining black-and-white (0/1) solutions (e.g., see Pereira et al. 2004; Navarrina et al. 2005; Paris et al. 2009; Lee et al. 2012). In the present study, we use the mass function shown in (13)<sub>1</sub>, in which the volume fraction of element  $e$ ,  $\tilde{\rho}_e$ , is defined in terms of the smooth Heaviside projection (Guest et al. 2004):

$$\tilde{\rho}_e = 1 - e^{-\beta\rho_e(\mathbf{z})} + \rho_e(\mathbf{z})e^{-\beta}, \quad (16)$$

where  $\beta \geq 0$  is a penalization parameter.

### 5.1 Piecewise vanishing stress constraint

The original vanishing constraint, displayed in (3), is an inequality constraint of the form  $g_j \leq 0$ . In order to use the AL method, we need to use a constraint of the form  $h_j = 0$ , which is computed using (42). The use of constraints  $h_j$  obtained from the traditional vanishing constraint may lead to negative values of the penalization term in the AL function (19), which in turn can temporarily deviate the optimization from the optima.<sup>5</sup> The nonlinear behavior of the stress constraints exacerbates this phenomenon, possibly leading to instability in the optimization algorithm. To overcome these difficulties, we establish the piecewise vanishing constraint, as shown below:

$$g_j(\mathbf{z}) = \begin{cases} \rho_j^p (\sigma_j^y / \sigma_{\text{lim}} - 1)^2 & \text{if } \sigma_j^y / \sigma_{\text{lim}} > 1 \\ 0 & \text{otherwise,} \end{cases} \quad (17)$$

where the exponent  $p$  is the SIMP penalization factor. This exponent factor  $p$  helps to regularize the behavior of the constraint by correlating it with the behavior of the local stiffness matrix as a function of the density. We denote this constraint as the *piecewise vanishing constraint* and use it in the optimization statement (13).

When compared with a vanishing constraint of the traditional form  $g_j(\mathbf{z}) = \rho_j(\sigma_j^y / \sigma_{\text{lim}} - 1)$ , squaring the term between parenthesis provides a more severe penalization to stresses that are much higher than  $\sigma_{\text{lim}}$  and alleviates the constraint for stresses closer to the stress limit. This allows a smoother transition to a design with lower overall stress during the optimization iterations, while preserving  $C^1(\mathbf{z})$  continuity<sup>6</sup>—an important characteristic for gradient-based

<sup>5</sup>As an example, suppose that for a given AL step we have  $g = -0.5$ ,  $\lambda = 1$ , and  $\mu = 1$ . For this combination of constraint values and AL parameters, we have that,  $h = \max(g, -\lambda/\mu) = \max(-0.5, -1) = -0.5$ , which yields  $P = \lambda h + \frac{1}{2}\mu h^2 = -3/8 < 0$ , where  $P$  is the penalization term of the AL function.

<sup>6</sup>The piecewise constraint given by (17) is  $C^1(\mathbf{z})$  because, for  $\sigma_j^y / \sigma_{\text{lim}} > 1$ ,  $g_j(\mathbf{z}) = \rho_j^p (\sigma_j^y / \sigma_{\text{lim}} - 1)^2$ , which is the finite composition of  $C^\infty$  functions in this domain, and for  $\sigma_j^y / \sigma_{\text{lim}} < 1$ ,  $g_j(\mathbf{z}) = 0$ , which is also  $C^\infty$ . Moreover, when  $\sigma_j^y / \sigma_{\text{lim}} = 1$ , both the value of  $\rho_j^p (\sigma_j^y / \sigma_{\text{lim}} - 1)^2$  and its first derivative with respect to  $\mathbf{z}$  are equal to zero, which is the same value of  $g_j(\mathbf{z})$  and its derivative with respect to  $\mathbf{z}$ , when  $\sigma_j^y / \sigma_{\text{lim}} < 1$ .

optimization. Appendix C presents numerical results that demonstrate the superiority of the results obtained with the piecewise vanishing constraint, as compared to those obtained using the traditional  $\varepsilon$ -relaxed stress constraint.

### 5.2 Stress Measure

Based on the  $qp$ -relaxation approach by (Bruggi 2008) (see (5)), we adopt the stress measure,

$$\tilde{\sigma}^v = \rho^{0.5} \sigma^v. \tag{18}$$

That is, we use  $p - q = 0.5$ . The stress measure,  $\tilde{\sigma}^v$ , is computed based on the apparent “local” von Mises stress (Duysinx and Bendsøe 1998a, b), which we compute based on the elastic properties of the solid material. Given that we use an Ersatz stiffness approach to obtain the stiffness matrices (e.g., see (14)), the apparent “local” von Mises stress,  $\sigma^v$ , stays finite as  $\rho \rightarrow 0$ . Because  $\sigma^v$  is finite, the stress measure given by (18) approaches zero as  $\rho \rightarrow 0$ . In addition, when  $\rho \rightarrow 1$ , the stress measure becomes equal to the apparent local von Mises stress,  $\sigma^v$ , of the solid material. The quantity  $\tilde{\sigma}^v$  is used for plotting and for the evolution of the parameter  $\gamma_e$ , as shown later. For further discussion on the difference between the apparent “local” von Mises stress and the stress measure, see Appendix B.

### 5.3 Augmented Lagrangian approach

We solve the optimization statement (13) using the aforementioned AL method. We introduce modifications in order to improve convergence towards a 0/1 solution and to improve the robustness of the method under mesh refinement or coarsening. The first modification consists of rewriting the mass function,  $m(\mathbf{z})$  (see (13)<sub>1</sub>), using weight factors  $\gamma_e$ . The second modification consists of multiplying the penalty term of the AL function by a scale factor  $\eta$ . The third modification consists of adding an interphase penalization,  $F(\mathbf{z})$ , to the AL function. As we will discuss in detail later, this interphase penalization aims to prevent small-scale features from appearing in the optimized topologies and it is only considered when we use continuation in the filter radius during the optimization steps. The corresponding AL function for the  $k$ th sub-problem reads as follows:

$$J^{(k)}(\mathbf{z}) = \sum_{e=1}^{N_e} \gamma_e^{(k)} \tilde{\rho}_e v_e + \eta \sum_{j=1}^{N_c} \left[ \lambda_j^{(k)} g_j(\mathbf{z}) + \frac{\mu^{(k)}}{2} g_j(\mathbf{z})^2 \right] + \delta F(\mathbf{z}), \tag{19}$$

where  $g_j(\mathbf{z})$  is defined in (17) and  $\delta = 1$  when the continuation in the filter radius is active, and  $\delta = 0$

otherwise. The first two modifications to the AL function will be discussed in the following two sections and the third modification will be discussed later.

### 5.4 Adaptive weight factors $\gamma_e$

Weight factors  $\gamma_e$ , which affect the objective function term in (19), help push the solution of the optimization problem towards black and white (0/1) and also help the optimizer to overcome local optima with high volume. This modification only affects the mass function and, as such, it is tailored to solve the mass minimization problem with local stress constraints given in (13). We present a heuristic argument to determine the evolution of weight factors  $\gamma_e$ , which is based on the effect of such factors on the AL function (19). In general, when  $\tilde{\sigma}_e^v > \sigma_{lim}$ , the behavior of the AL (19) tends to be dominated by the penalty term, and when  $\tilde{\sigma}_e^v < \sigma_{lim}$ , the behavior tends to be dominated by the objective function term. To increase the relevance of the penalty term when  $\tilde{\sigma}_e^v > \sigma_{lim}$ , we lower the value of  $\gamma_e$ , which only affects the volume of element  $e$ . Similarly, to increase the relevance of the objective function term when  $\tilde{\sigma}_e^v < \sigma_{lim}$ , we increase the value of  $\gamma_e$  for that element.

These observations suggest the use of an adaptive  $\gamma_e$  for each element. Thus, we suggest a heuristic expression for weight factors  $\gamma_e$  as a function of the stress measure  $\tilde{\sigma}_e^v$  defined in Eq. (18). The update of parameters  $\gamma_e$  for  $e = 1, \dots, N_e$  is given by the following:

$$\gamma_e^{(k+1)} = \begin{cases} \max(a_1 \gamma_e^{(k)} + b_1, \gamma_L) & \text{if } \tilde{\sigma}_e^v > \sigma_{lim} \\ \min(a_2 \gamma_e^{(k)} + b_2, \gamma_U) & \text{otherwise,} \end{cases} \tag{20}$$

where  $\gamma_L$  and  $\gamma_U$  are the lower and upper bounds for  $\gamma_e$ , respectively. Parameters  $a_1, a_2, b_1$ , and  $b_2$  are obtained empirically, with the only requirement being that  $\gamma_e$  decreases if  $\tilde{\sigma}_e^v > \sigma_{lim}$  and increases otherwise. If the aforementioned requirements are met, our experience has shown that the optimization results are relatively insensitive to the choice of the numerical constants in (20). Figure 3 shows an example of the evolution of  $\gamma_e^{(k)}$  for successive sub-problems,  $k$ , following the update function displayed in (20), for a case in which the condition  $\tilde{\sigma}_e^v > \sigma_{lim}$  is always true (blue curve) and for a case in which the converse condition is always true (red curve). These curves are shown for illustrative purposes only because the evolution of  $\gamma_e^{(k)}$  is, in general, not monotonic and depends on the value of  $\tilde{\sigma}_e^v / \sigma_{lim}$  in each sub-problem,  $k$ . As shown in the figure, parameters  $\gamma_e$  decrease when  $\tilde{\sigma}_e^v > \sigma_{lim}$  and increase otherwise. The weight factors,  $\gamma_e^{(k)}$ , are kept constant for each AL step,  $k$ , and thus the AL function remains differentiable during the solution of each sub-problem. Appendix D investigates the effect of using parameters  $\gamma_e$

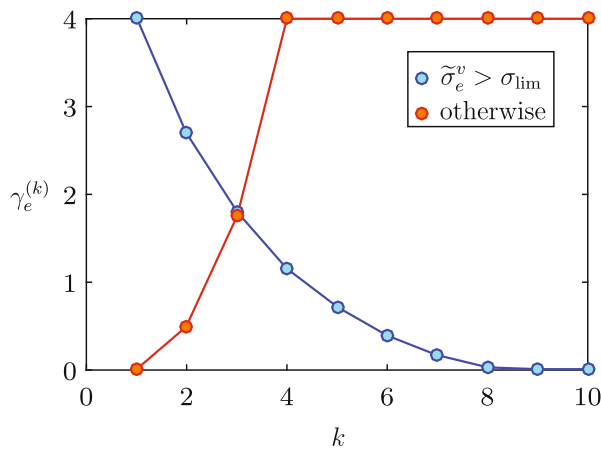


**Fig. 3** Values of  $\gamma_e^{(k)}$  for successive values of  $k$  considering both  $\tilde{\sigma}_e^v$  being above and below  $\sigma_{\text{lim}}$ . The values of  $\gamma_e^{(k)}$  are obtained according to Eq. (20), with  $a_1 = 0.7$ ,  $a_2 = 2.5$ ,  $b_1 = -0.1$ ,  $b_2 = 0.5$ ,  $\gamma_L = 0$ , and  $\gamma_U = 4$

in the quality of the optimization results for an  $L$ -bracket domain for various mesh sizes.

The introduction of parameters  $\gamma_e^{(k)}$  adapts the objective function term of the AL (19), which modifies the original optimization statement for intermediate AL sub-problems. However, as the optimization converges,  $\tilde{\sigma}_e^v$  tends to values lower than or equal to  $\sigma_{\text{lim}}$ , which means that  $\gamma_e^{(k)} \rightarrow \gamma_U$  (see Fig. 3), leading to a uniform distribution of  $\gamma_e$ . Consequently, as the optimization converges, the objective function is basically multiplied by a constant term  $\gamma_U$ , and thus, the optima points of the modified optimization problem are the same as those of the original problem.

### 5.5 Scale factor $\eta$

Progress toward a feasible solution using the traditional AL method depends on the ratio between the original objective function and the penalty term of the AL function. The magnitude of the penalty term is highly dependent on the number of constraints. In the context of topology optimization with local stress constraints, the number of constraints increases when the mesh is refined and decreases when the mesh is coarsened. Through numerical experimentation, we found that if the objective-to-penalty ratio in the AL function is kept approximately constant and independent of the number of constraints, our AL formulation leads to consistent optimization results as the underlying mesh is refined or coarsened. To preserve this ratio as the mesh is refined or coarsened, we multiply the penalty term by a scale factor  $\eta$  (e.g., see (19)), which is given by the following:

$$\eta = 1/N_c, \quad (21)$$

where  $N_c$  is the number of constraints. The proposed scale factor  $\eta$  helped us obtain consistent optimization results for a variety of problems solved in the present study, in which the number of constraints ranged between a few thousands to over one million. In Appendix E, we present some numerical results that demonstrate the effect of having scale factor  $\eta$  in the quality of the optimization results.

## 6 Sensitivity analysis

The stress-constrained topology optimization problem discussed in this section is solved using gradient-based optimization algorithms. In order to do so, sensitivity information for the AL function (19) is required. The sensitivity of the AL function is computed using the chain rule as follows:

$$\frac{dJ^{(k)}}{dz_j} = \sum_{i=1}^{N_e} \frac{\partial J^{(k)}}{\partial \rho_i} \frac{d\rho_i}{dz_j} = \sum_{i=1}^{N_e} \frac{\partial J^{(k)}}{\partial \rho_i} P_{ij}. \quad (22)$$

The term  $P_{ij}$  in (22) is obtained from the relation  $\rho(\mathbf{z}) = \mathbf{Pz}$  and the term  $\partial J^{(k)}/\partial \rho_i$  is obtained using (19), as follows<sup>7</sup>:

$$\frac{\partial J^{(k)}}{\partial \rho_i} = \frac{\partial}{\partial \rho_i} \sum_{e=1}^{N_e} \gamma_e \tilde{\rho}_e v_e + \eta \frac{\partial}{\partial \rho_i} \sum_{j=1}^{N_c} \left[ \lambda_j g_j(\mathbf{z}) + \frac{\mu}{2} g_j(\mathbf{z})^2 \right]. \quad (23)$$

For simplicity in the notation, we have dropped the superscript  $k$  in (23) and in the subsequent equations of this section. The first part of (23), which is related to the objective function, is computed as follows:

$$\frac{\partial}{\partial \rho_i} \sum_{e=1}^{N_e} \gamma_e \tilde{\rho}_e v_e = \gamma_i \frac{\partial \tilde{\rho}_i}{\partial \rho_i} v_i = \gamma_i \left( \beta e^{-\beta \rho_i(\mathbf{z})} + e^{-\beta} \right) v_i. \quad (24)$$

The second part of (23), which is related to the penalty term, is computed as follows:

$$\frac{\partial}{\partial \rho_i} \sum_{j=1}^{N_c} \left[ \lambda_j g_j(\mathbf{z}) + \frac{\mu}{2} g_j(\mathbf{z})^2 \right] = \sum_{j=1}^{N_c} \left[ \lambda_j + \mu g_j(\mathbf{z}) \right] \frac{\partial g_j(\mathbf{z})}{\partial \rho_i}. \quad (25)$$

<sup>7</sup>Because the interphase penalization  $F(\mathbf{z})$  in (19) is only used when we apply continuation on the filter radius, we have decided not to include it in the current derivation.

Using (17) and (42), the non-zero part of the sensitivity of constraints  $h_j$  is determined as follows:

$$\begin{aligned} \frac{\partial h_j(\mathbf{z})}{\partial \rho_i} &= \frac{\partial}{\partial \rho_i} \left[ \rho_j^p (\sigma_j^y / \sigma_{\text{lim}} - 1)^2 \right] \\ &= p \rho_j^{p-1} \delta_{ij} (\sigma_j^y / \sigma_{\text{lim}} - 1)^2 \\ &\quad + \frac{2 \rho_j^p}{\sigma_{\text{lim}}} (\sigma_j^y / \sigma_{\text{lim}} - 1) \left( \frac{\partial \sigma_j^y}{\partial \mathbf{u}} \right)^T \frac{\partial \mathbf{u}}{\partial \rho_i}, \end{aligned} \tag{26}$$

where  $\delta_{ij}$  is the Kronecker delta operator and  $\mathbf{u}$  is the displacement vector obtained from the equilibrium equation  $\mathbf{K}\mathbf{u} = \mathbf{f}$ . The last part of (26) corresponds to the sensitivity of the von Mises stress for the  $j$ th stress constraint. The adjoint method is used herein to avoid the expensive computation of  $\partial \mathbf{u} / \partial \rho_i$  (Bendsøe and Sigmund 2003; Christensen and Klarbring 2008). Differentiating the aforementioned equilibrium equation with respect to the design variables, and assuming that  $\mathbf{f}$  is independent of the design variables, we obtain:

$$\frac{\partial \mathbf{K}}{\partial \rho_i} \mathbf{u} + \mathbf{K} \frac{\partial \mathbf{u}}{\partial \rho_i} = \mathbf{0}. \tag{27}$$

Substituting (26) into (25) and adding the expression in (27) multiplied by the adjoint vector,  $\boldsymbol{\xi}$ , leads to the following:

$$\begin{aligned} &\frac{\partial}{\partial \rho_i} \sum_{j=1}^{N_c} \left[ \lambda_j g_j(\mathbf{z}) + \frac{\mu}{2} g_j(\mathbf{z})^2 \right] \\ &= \sum_{j=1}^{N_c} \left[ \lambda_j + \mu g_j(\mathbf{z}) \right] p \rho_j^{p-1} \delta_{ij} (\sigma_j^y / \sigma_{\text{lim}} - 1)^2 \\ &\quad + \sum_{j=1}^{N_c} \left[ \lambda_j + \mu g_j(\mathbf{z}) \right] \frac{2 \rho_j^p}{\sigma_{\text{lim}}} (\sigma_j^y / \sigma_{\text{lim}} - 1) \left( \frac{\partial \sigma_j^y}{\partial \mathbf{u}} \right)^T \frac{\partial \mathbf{u}}{\partial \rho_i} \\ &\quad + \boldsymbol{\xi}^T \left( \frac{\partial \mathbf{K}}{\partial \rho_i} \mathbf{u} + \mathbf{K} \frac{\partial \mathbf{u}}{\partial \rho_i} \right). \end{aligned} \tag{28}$$

Collecting all terms in (28) that multiply  $\partial \mathbf{u} / \partial \rho_i$  and choosing  $\boldsymbol{\xi}$  such that these terms vanish from the sensitivity evaluation allows rewriting (28) as follows:

$$\begin{aligned} &\frac{\partial}{\partial \rho_i} \sum_{j=1}^{N_c} \left[ \lambda_j g_j(\mathbf{z}) + \frac{\mu}{2} g_j(\mathbf{z})^2 \right] \\ &= [\lambda_i + \mu g_i(\mathbf{z})] p \rho_i^{p-1} (\sigma_i^y / \sigma_{\text{lim}} - 1)^2 + \boldsymbol{\xi}^T \frac{\partial \mathbf{K}}{\partial \rho_i} \mathbf{u}, \end{aligned} \tag{29}$$

where  $\boldsymbol{\xi}$  is the solution to the following adjoint problem:

$$\mathbf{K} \boldsymbol{\xi} = - \sum_{j=1}^{N_c} \left[ \lambda_j + \mu g_j(\mathbf{z}) \right] \frac{2 \rho_j^p}{\sigma_{\text{lim}}} (\sigma_j^y / \sigma_{\text{lim}} - 1) \frac{\partial \sigma_j^y}{\partial \mathbf{u}}. \tag{30}$$

The last term in (29) is obtained as  $\boldsymbol{\xi}^T \frac{\partial \mathbf{K}}{\partial \rho_i} \mathbf{u} = \boldsymbol{\xi}_i^T \frac{\partial \mathbf{k}_i}{\partial \rho_i} \mathbf{u}_i$ , where  $\boldsymbol{\xi}_i$ ,  $\mathbf{k}_i$ , and  $\mathbf{u}_i$  refer to element-wise quantities.

Because we compute the element stiffness matrices using (14)<sub>2</sub>, then

$$\frac{\partial \mathbf{k}_i}{\partial \rho_i} = p(1 - \epsilon) \rho_i^{p-1} \mathbf{k}_0. \tag{31}$$

By substituting (24), (29), and (31) into (23), we obtain the following:

$$\begin{aligned} \frac{\partial J^{(k)}}{\partial \rho_i} &= \gamma_i \left( \beta e^{-\beta \rho_i(\mathbf{z})} + e^{-\beta} \right) v_i \\ &\quad + \eta \left[ (\lambda_i + \mu g_i(\mathbf{z})) p \rho_i^{p-1} (\sigma_i^y / \sigma_{\text{lim}} - 1)^2 \right. \\ &\quad \left. + p(1 - \epsilon) \rho_i^{p-1} \boldsymbol{\xi}_i^T \mathbf{k}_0 \mathbf{u}_i \right], \end{aligned} \tag{32}$$

which is substituted into (22) to obtain the final expression for the sensitivity of the AL function (19), i.e.:

$$\begin{aligned} \frac{dJ^{(k)}}{dz_j} &= \sum_{i=1}^{N_e} \gamma_i \left( \beta e^{-\beta \rho_i(\mathbf{z})} + e^{-\beta} \right) v_i P_{ij} \\ &\quad + \eta \sum_{i=1}^{N_e} \left[ (\lambda_i + \mu g_i(\mathbf{z})) p \rho_i^{p-1} (\sigma_i^y / \sigma_{\text{lim}} - 1)^2 \right. \\ &\quad \left. + p(1 - \epsilon) \rho_i^{p-1} \boldsymbol{\xi}_i^T \mathbf{k}_0 \mathbf{u}_i \right] P_{ij}. \end{aligned} \tag{33}$$

Note that using the adjoint vector,  $\boldsymbol{\xi}$ , obtained from (30) greatly reduces the cost of sensitivity evaluation as compared to evaluating (22)–(26) directly, which requires computation of  $\partial \mathbf{u} / \partial \rho_i$  for  $i = 1, \dots, N_c$ .

## 7 Implementation details

Here, we present some implementation details for the proposed AL-based formulation. We start by describing a strategy that we implement for addressing the non-convexity of the optimization problem, followed by a description of a continuation strategy that we use for the filter radius. We finalize by providing a pseudo-code to summarize the AL-based formulation to solve consistent stress-constrained topology optimization problems.

### 7.1 Addressing non-convexity

The nonlinear behavior of the stress constraints combined with the disconnected regions in the solution space illustrated by Fig. 1b causes the optimization problem to become non-convex. Consequently, it is common for optimization algorithms to get trapped in local optima. In addition, the nonlinear behavior of the problem causes the solutions to differ significantly when initial parameters of the problem are changed and when different discretizations of the same underlying domain are used.

A common strategy when using the AL method for non-convex problems is to restart the values of  $\mu$  and  $\lambda_j$  when

the optimization stagnates<sup>8</sup> (Bertsekas 1996, 1999; Nocedal and Wright 2006). In the present study, we implement that strategy, but we also restart the values of weight factors  $\gamma_e$  when the optimization stagnates. Once these parameters are restarted, we conduct additional optimization iterations until reaching convergence.

This approach allows us to achieve better results, i.e., designs with lower mass ratio than that obtained when these parameters are not restarted. For practical purposes, we allow these parameters to be restarted up to four times for the 2D examples and up to two times for the 3D examples. The effect of restarting these parameters in the quality of the optimization results is demonstrated in Appendix F for a particular optimization problem.

## 7.2 Achieving stress constraint satisfaction

The piecewise vanishing constraint given in (17) has a null gradient whenever its associated stress constraint is satisfied. The null gradient slows down the convergence rate when the optimization is close to an optimal point, which prevents us from achieving strict stress constraint satisfaction. In order to improve numerical stability and enable a strict stress constraint satisfaction, we lower the stress limit of the constraints that are not satisfied when the optimization is close to convergence. We lower the stress limit,  $\sigma_{\text{lim}}^e$ , of each element gradually to preserve the stability of the optimization algorithm, and this is achieved by using the weight factors,  $\gamma_e$ , as an indicator of constraint violation. Notice that the weight factors can be considered as an indicator of constraint violation that changes gradually between each AL sub-problem. Therefore, we define an artificial stress limit as follows:

$$\sigma_{\text{lim}}^e = \left( \frac{\gamma_U \sigma_{\text{lim}}^R + (1 - \sigma_{\text{lim}}^R) \gamma_e^{(k)} - \gamma_L}{\gamma_U - \gamma_L} \right) \sigma_{\text{lim}}, \quad (34)$$

in which  $\sigma_{\text{lim}}^R$  is the maximum reduction of the stress limit. The factor  $\sigma_{\text{lim}}^R$  is successively lowered at each sub-problem, according to the following expression:

$$(\sigma_{\text{lim}}^R)^{(k+1)} = \max(1.25(\sigma_{\text{lim}}^R)^{(k)} - 0.26, 0.65). \quad (35)$$

Equation (34) shows that  $\sigma_{\text{lim}}^e \rightarrow \sigma_{\text{lim}}$  when the constraint associated with element  $e$  is satisfied over successive AL

sub-problems, which happens because  $\gamma_e^{(k)} \rightarrow \gamma_U$  as the solution converges. Thus, as the sub-problems converge to an optimum point, we recover the original optimization problem. The artificial stress limits,  $\sigma_{\text{lim}}^e$ , similar to the weight factors,  $\gamma_e^{(k)}$ , are kept constant for each AL step,  $k$ , and thus the AL function remains differentiable during the solution of each sub-problem.

## 7.3 Continuation on filter radius

In order to achieve optimization results with lower mass ratio and well-defined material boundaries (i.e., 0/1 designs), we use continuation on the filter radius during the optimization steps. In the remainder of this paper, we refer to such continuation strategy as *filter reduction*. In this study, we propose a filter reduction scheme in which the filter radius of element  $e$  is a function of its density. That is, we conduct a local density-based modification of the convolution function used for the original filter (see (15)). Unlike the traditional filter schemes that use one filter radius, which controls the length scale of the final designs, the proposed filter reduction strategy allows each element to have an individual filter radius, which yields optimization results with well-defined material boundaries. The filter reduction procedure used in this study is as follows:

1. A density measure of each element,  $\bar{\rho}_e$ , is obtained by applying the initial filter to the design variables  $\mathbf{z}$ . That is,  $\bar{\rho} = \mathbf{P}_0 \mathbf{z}$ , where  $\mathbf{P}_0$  is the initial filter matrix.
2. The filter radius of an element is then scaled using a ratio equal to the maximum between the filtered density and  $\rho_{\text{ref}} = 0.7$ . That is, the filter radius of element  $e$  is updated as  $r_e^{i+1} = \max(\bar{\rho}_e, \rho_{\text{ref}}) r_e^i$ . A lower bound,  $r_{\text{min}}$ , is used for the element filter radius in order to prevent the appearance of checkerboards.
3. The new filter matrix is computed using the filter radius of each element,  $r_e^{i+1}$ .

The filter reduction is performed after the optimization achieves a certain level of stagnation. The density measure described in step 1 is always obtained using the original filter, in order to retain information about the defined minimum length scale; yet, the reduced filter radius is computed using the previously updated filter radius to achieve a well-defined density map. In our implementation, once the condition  $\text{Change} < \text{tol}$  is first met, the filter radius is updated every 10 optimization steps. The value of  $\rho_{\text{ref}} = 0.7$  in step 2 is set to achieve a gradual reduction of the filter radius and to prevent numerical instabilities, which may occur if the filter radius reduces too fast.

In our implementation, we stop reducing the element filter radius when  $n_{i+1}/n_i > 0.9$ , in which  $n_i$  and  $n_{i+1}$  correspond to the number of non-zero entries of filter matrices  $\mathbf{P}_i$  and  $\mathbf{P}_{i+1}$ , respectively (i.e., when two

<sup>8</sup>Stagnation is reached when the average change in the design variables between two consecutive iterations is smaller than a given tolerance, i.e., when  $\text{Change} < \text{tol}$  (cf. Algorithm 2) and the constraints are yet not satisfied.

consecutive filter matrices,  $\mathbf{P}_i$  and  $\mathbf{P}_{i+1}$ , have similar topology<sup>9</sup>). We use the number of non-zero entries as a criterion of similarity because, as can be seen in (15), as the filter reduction procedure converges, the number of non-zero entries of filter matrices  $\mathbf{P}_i$  and  $\mathbf{P}_{i+1}$  will be similar. In addition, whenever the optimization parameters are restarted, the filter radius is also restarted to its initial value, which helps to remove unwanted small-scale features from the optimized topologies.

The filter reduction scheme described above can be implemented efficiently, using the previously stored filter matrix, as shown in Algorithm 1. Although efficient, the filter reduction procedure described herein requires storage of the original filter matrix,  $\mathbf{P}_0$ , as well as the reduced filter matrix,  $\mathbf{P}$ , which can substantially increase the memory requirements of the algorithm.

The interphase penalization in (36) associates a non-zero value to the interphasial regions of the structure and is computed using the original filter with the original radius defined for the length-scale control. The reason for using the original filter to compute this penalization term is to retain information of the original length scale. Features with a characteristic size smaller than the original length scale will have a higher ratio of (interphase penalization)/stiffness, and, with that, they are more penalized, and, consequently, disfavored by the optimizer. As a result, adding the interphase penalization (36) to the AL function (19), when the filter reduction scheme is used, tends to prevent small artifacts from appearing in the optimized topologies. The interphase penalization,  $F(\mathbf{z})$ , is introduced in the later stages of the optimization steps, when the problem has stagnated. The introduction of  $F(\mathbf{z})$  alters the AL function, but the optimization problem remains stable.

---

**Algorithm 1** Filter reduction procedure

---

```

1: procedure FILTER_REDUCTION( $\mathbf{P}_0, \mathbf{P}, \mathbf{z}$ )
2:    $\bar{\rho} = \mathbf{P}_0 \mathbf{z}$ 
3:   Ratio =  $\max(\bar{\rho}, 0.7)$ ;
4:   for each row  $i$  of matrix  $\mathbf{P}$  do
5:     for each column  $j$  of matrix  $\mathbf{P}$  do
6:        $P_{ij} = \max(1 - \sqrt[s]{1 - P_{ij}/P_{ii}} \times \text{Ratio}_i, 0)^s$ ;           ▷ Reduce radius of element  $i$  by  $\text{Ratio}_i$ 
7:     end for
8:      $\text{Renorm} = \sum_j P_{ij}$ ;
9:     for each column  $j$  of matrix  $\mathbf{P}$  do
10:       $P_{ij} = P_{ij}/\text{Renorm}$ ;
11:    end for
12:  end for
13:  return  $\mathbf{P}$ 
14: end procedure

```

---

When the filter reduction scheme is used, the filter radius of each element is reduced independently. As a result, small-scale artifacts tend to appear in the optimized topologies. In order to address this issue, as soon as the first filter reduction is performed, we add the interphase penalization,

$$F(\mathbf{z}) = \frac{2}{N_e} \sum_{e=1}^{N_e} \bar{\rho}_e (1 - \bar{\rho}_e^3), \tag{36}$$

to the adapted AL function, by setting  $\delta = 1$  in (19).<sup>10</sup> Notice that, if  $\delta = 0$ , then this term is not present.

<sup>9</sup>When two consecutive filter matrices have similar topology, it indicates that the material distribution between two consecutive iterations has not changed significantly. Alternatively, we could use a criterion based on  $\|\mathbf{P}_{i+1} - \mathbf{P}_i\|$  to stop the filter reduction, but this means storing both  $\mathbf{P}_i$  and  $\mathbf{P}_{i+1}$ , which requires a substantial amount of RAM memory.

<sup>10</sup>The function defined in Eq. (36) is not unique, and other functions such as  $\rho(1 - \rho)$  can be used for the same purpose. We choose the function in Eq. (36) because its slight asymmetry with respect to  $\rho = 0.5$  tends to favor designs with lower weight.

For implementation purposes, we normalize the interphase penalization (36) with respect to its value at the moment of the first filter reduction. That is because, depending on the problem being solved, its magnitude can dominate the problem, or it can be too small to remove small artifacts from the optimized topologies.

Whenever the optimization is restarted, the original filter is restored and the interphase penalization is removed from (19). When the solution starts to converge once more, the interphase penalization is added back to the AL function (19), and the entire optimization procedure continues.

### 7.4 Optimization algorithm

A pseudo-code summarizing the optimization procedure described above is presented in Algorithm 2. The algorithm contains three main loops. The most outer loop (line 6) is used to restart the values of  $\lambda^{(k)}$ ,  $\mu^{(k)}$ , and  $\gamma^{(k)}$  if the optimization stagnates. The AL steps are conducted in

**Algorithm 2** Stress-constrained topology optimization based on the AL method

---

```

1: procedure MODIFIED AUGMENTED LAGRANGIAN
2:    $\mathbf{z}^{(1)} =$  initial guess
3:   Change = 1;
4:    $k = 1$ ;
5:   outerIter = 1;
6:   while ( $\max(\tilde{\sigma}_e^v) > \sigma_{\text{lim}}$  and  $\text{outerIter} \leq \text{maxOuterIter}$ ) do  $\triangleright$  Restart modified AL (Section 7.1)
7:      $\boldsymbol{\lambda}^{(k)} = \boldsymbol{\lambda}^{(1)}$ ;
8:      $\mu^{(k)} = \mu^{(1)}$ ;
9:      $\boldsymbol{\gamma}^{(k)} = \mathbf{0}$ ;
10:    while ( $(\text{Change} > \text{tol}$  or  $\max(\tilde{\sigma}_e^v) > \sigma_{\text{lim}})$  and  $k < \text{MaxIter}$ ) do
11:      Use MMA to find  $\mathbf{z}^{(k+1)}$  that minimizes  $J^{(k)}(\mathbf{z})$ , starting at  $\mathbf{z}^{(k)}$ ;  $\triangleright$  Eq. (19),  $J^{(k)}(\mathbf{z})$ 
12:      Compute  $\sigma_e^v$  using  $\mathbf{u} = \mathbf{K}^{-1}(\mathbf{z}^{(k+1)})\mathbf{f}$ ,  $e = 1, \dots, N_e$ ;
13:      Update  $\lambda_j^{(k+1)}$ ,  $j = 1, \dots, N_e$ ;  $\triangleright$  Eq. (11),  $\lambda_j^{(k+1)} = \lambda_j^{(k)} + \mu^{(k)}g_j(\mathbf{z}^{(k)})$ 
14:      Update  $\gamma_e^{(k+1)}$ ,  $j = 1, \dots, N_e$ ;  $\triangleright$  Eq. (20),  $\gamma_e^{(k+1)}$  adaptation
15:      Change =  $\text{sum}(|\mathbf{z}^{(k)} - \mathbf{z}^{(k+1)}|)/N_e$ ;
16:      if Change < tol then
17:         $\mu^{(k+1)} = 1.05\mu^{(k)}$ ;
18:         $\gamma_U = \max(0.95\gamma_U, 1)$ ;
19:         $(\sigma_{\text{lim}}^R)^{(k+1)} = \max(1.25(\sigma_{\text{lim}}^R)^{(k)} - 0.26, 0.65)$   $\triangleright$  Equation (35)
20:        if Filter Reduction is used then
21:          Start Filter Reduction procedure  $\triangleright$  Algorithm 1
22:        end if
23:      else
24:         $\mu^{(k+1)} = \mu^{(k)}$ ;
25:      end if
26:      if (Change < outerTol and  $\text{outerIter} < \text{maxOuterIter}$ ) then
27:        break inner loop;  $\triangleright$  Unless it is the last outer loop
28:      end if
29:       $k = k + 1$ ;
30:    end while
31:    outerIter = outerIter + 1;
32:  end while
33: end procedure

```

---

the inner loop starting on line 10. The most inner loop, which is located on line 11, is used to run a few MMA iterations (Svanberg 1987) to approximately minimize the AL function (19) at each AL step  $k$  (i.e., line 11 corresponds to the solution of the  $k$ th AL sub-problem). Once the algorithm exits the loop on line 11, the von Mises stress distribution is obtained for each element  $e$  (line 12), followed by an update of Lagrange multiplier estimators  $\lambda_j^{(k)}$  and weight factors  $\gamma_e^{(k)}$ , respectively (lines 13–14). In order to speed-up convergence, when the average step size is lower than the tolerance (line 16), parameters  $\mu^{(k)}$ ,  $\gamma_U$ , and  $(\sigma_{\text{lim}}^R)^{(k)}$  are updated to help drive the design towards a feasible solution. If the filter reduction strategy is used, then the filter reduction procedure described in Algorithm 1 is applied (lines 20–22). If changes in the design variables

are still significant, penalty parameter  $\mu^{(k+1)}$  remains unchanged (line 24). Finally, if the optimization stagnates before the stress constraints have been satisfied, the inner loop breaks (line 26), and the algorithm goes back to line 6, where the values of  $\boldsymbol{\lambda}^{(k)}$ ,  $\mu^{(k)}$ , and  $\boldsymbol{\gamma}^{(k)}$  are restarted.

## 8 Numerical results

This section presents numerical results obtained using a MATLAB implementation of the proposed method. In order to facilitate the reproduction of the results presented in this paper, Table 1 displays the initial values for  $\mu^{(k)}$ ;  $\lambda_j^{(k)}$ ,  $j = 1, \dots, N_e$ ; and  $\gamma_e^{(k)}$ ,  $e = 1, \dots, N_e$ , as well as

other numerical parameters considered.<sup>11</sup> Unless otherwise specified, the parameters in Table 1 are used in all examples.

We present several 2D and 3D examples to illustrate some of the attributes of the present formulation. The 2D designs are useful for problems in which plane stress assumptions are acceptable, and the 3D designs are of interest for most engineering applications in which a 2D model is insufficient. With the growing interest in additive manufacturing technologies to prototype increasingly complex structures (Wong and Hernandez 2012; Gibson et al. 2015), it is imperative to have reliable design tools for 3D optimized structures that are able to withstand their applied loads. Through the 3D examples, we show that the current formulation can be conceived as a first step in that direction.

The mathematical formulation (13) for the mass minimization problem with stress constraints admits a trivial optimum solution corresponding to a structure with no mass (i.e.,  $\rho = 0$  everywhere). However, such trivial solutions are of no interest because they have no practical meaning. We are interested in optimized solutions with non-zero mass. As such, the results presented herein correspond to optimized solutions to statement (13), which have non-zero mass. Furthermore, all solutions presented hereafter satisfy the stress constraints in every evaluation point.

## 8.1 Diagonal square

In this example, we use our adapted AL formulation to solve step-by-step the diagonal square problem introduced previously. The geometry of the diagonal square problem is shown in Fig. 1a and the feasible design domain in Fig. 1b. The initial parameters that we use to solve this problem are those of Table 1, except for  $\lambda_j^{(1)}$  and  $\mu^{(1)}$ , which for this example are taken as 1 and 10, respectively.

We show some of the intermediate optimization iterations for various AL sub-problems in Fig. 4. For the first AL sub-problem (i.e., for  $k = 1$ ), we start with  $(\rho_1, \rho_2) = (0.5, 0.6)$ , which we choose to break the symmetry of this particular optimization problem around the line  $\rho_1 = \rho_2$ . The black circles in Fig. 4a and in the subsequent sub-figures correspond to the intermediate optimization iterations for each AL sub-problem (i.e., each of the MMA iterations used to minimize the  $k$ th AL sub-problem). The results show that for the fourth AL sub-problem, the solution is already close to a global optimum of the original optimization problem. That is, our AL-based framework is able to reach inside the degenerated regions of the feasible design space shown in Fig. 1b.

<sup>11</sup>In addition to all parameters shown in Table 1, the MMA parameters (Svanberg 1987) used in all examples for the minimization of the AL sub-problems are  $asyinit = 0.2$ ,  $asyinc = 1.2$ ,  $asydec = 0.7$ ,  $move = 0.1$ .

## 8.2 2D L-bracket

This example presents the topology optimization results for an L-bracket problem, whose geometry is depicted in Fig. 5. As shown in Fig. 5, the L-bracket is fixed at the top and loaded at the free end with a load,  $P$ , that is distributed along a distance  $d$ . The material properties, geometry, and loading conditions used in this example are adopted from a study by Emmendoerfer and Fancello (2016), and are used for comparison purposes only. The input parameters used to solve this problem are shown in Table 2.

The material distributions and normalized von Mises stress maps,<sup>12</sup> obtained from the stress-constrained topology optimization formulation presented in this study, are shown in Table 3. The results are obtained for various mesh sizes (16,384, 160,000, and 500,000 regular Q4 elements) and regularization techniques (linear filter, polynomial filter, Heaviside projection, and filter reduction). As observed in all the results, the topology optimization formulation presented in Section 5 is able to remove material from the reentrant corner and achieve designs that satisfy the stress constraints to the desired stress limit. All results shown in Table 3 are converged; yet, they are all mesh-dependent, which is expected due to the non-convexity of the optimization statement (13).

The first two columns of Table 3 correspond to the results obtained using a linear filter and a polynomial filter, respectively. The topologies obtained using the linear filter quickly degenerate as the size of the mesh increases, leading to structures that are clearly sub-optimal. In contrast, the topologies obtained with the polynomial filter are in general well-defined; yet, they contain thin members, especially for the coarsest mesh. Although the results obtained using the polynomial filter are better than those obtained using the linear filter, we still observe some irregular members for the polynomial filter case (e.g., see results for 160,000 constraints), especially close to the bottom left portion of the bracket, which appears to be sub-optimal.

Another regularization technique that we investigate is based on the Heaviside projection by Guest et al. (2004) and used by Kiyono et al. (2016) in the context of stress-constrained topology optimization. To obtain the results based on the Heaviside projection, we use a continuation strategy on parameter  $\beta$ , such that we start with  $\beta = 0$  until the optimization iterations stagnate for the first time and then we gradually increase  $\beta$  by 2 every 10 iterations until reaching a maximum value of 30. The optimized topologies obtained using this method are shown on the

<sup>12</sup>The stress shown in this example, as well as those shown in subsequent examples, is the stress measure  $\tilde{\sigma}_e^v$  (18) normalized with respect to the stress limit,  $\sigma_{lim}$ .

**Table 1** Numerical parameters used to solve all problems in the present study

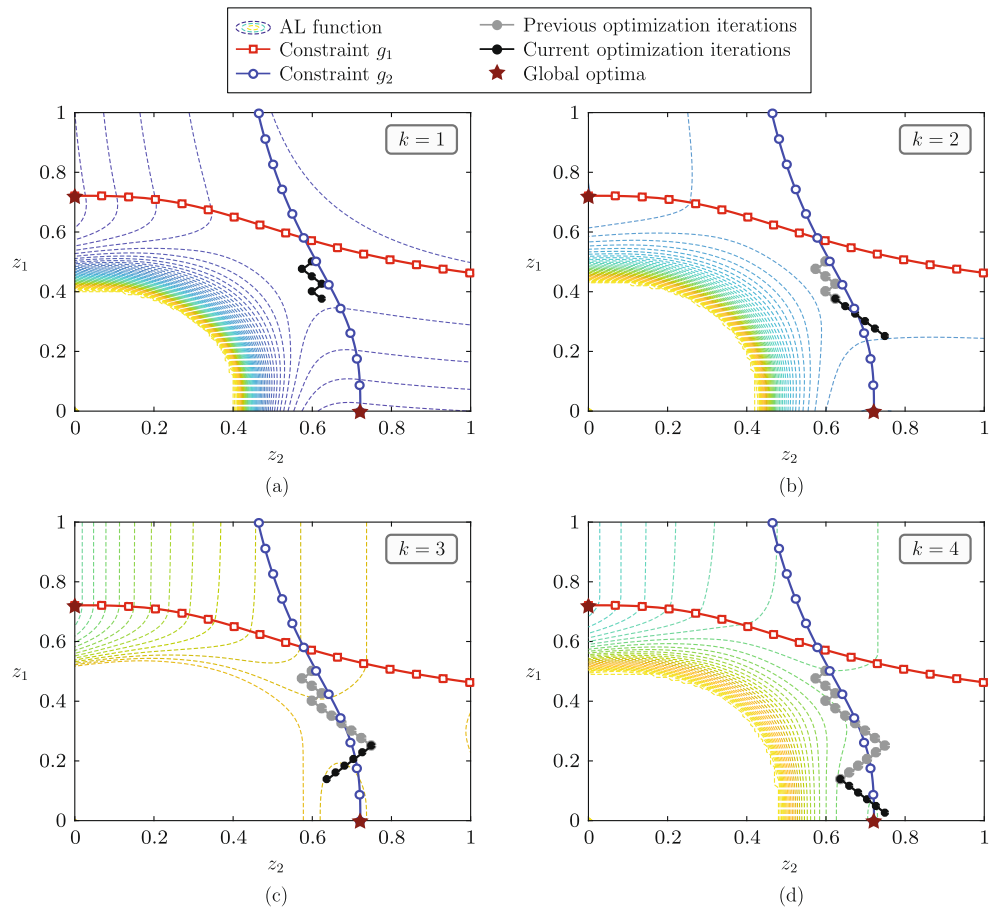
Parameter	Description	Value
$\lambda_j^{(1)}$	Initial Lagrange multipliers	300
$\mu^{(1)}$	Initial penalization factor	5000
$\gamma_e^{(1)}$	Initial weight factors	0.0
$\alpha$	Penalty factor updating parameter	1.05
$p$	SIMP penalization	3
$\beta$	Heaviside mass penalization	3
$\mathbf{z}^{(1)}$	Initial guess	0.5
$\epsilon$	Ersatz stiffness	$10^{-6}$
$a_1, a_2, b_1, b_2$	Weight factor update parameters	0.7, 2.5, -0.1, 0.5
$\gamma_L, \gamma_U$	Weight factor lower and upper limit	0, 4
tol	Tolerance of the step size	0.0005
outerTol	Tolerance for the restart of the AL parameters	$0.2 \text{ tol}$
maxOuterIter	Maximum number of restarts	4 (2D) or 2 (3D)

third column of Table 3. As illustrated by the results, the Heaviside projection method performs well for small mesh sizes, leading to clear material boundaries. However, as we increase the number of elements, we obtain large regions of gray resulting from the instability caused by the large value of the Heaviside penalization factor,  $\beta$ . Thus, as compared to all other methods investigated in this study, the Heaviside

projection method required the largest number of iterations to converge.

The last set of results (fourth column of Table 3) are those obtained based on the filter reduction technique introduced in this paper. As demonstrated by these results, the filter reduction strategy led to the best designs (i.e., the lightest structures with clearer material representation) among all

**Fig. 4** Intermediate optimization iterations for the AL sub-problem,  $k$ , corresponding to the diagonal square problem: **a**  $k = 1$ ; **b**  $k = 2$ ; **c**  $k = 3$ ; and **d**  $k = 4$  (online version in color)



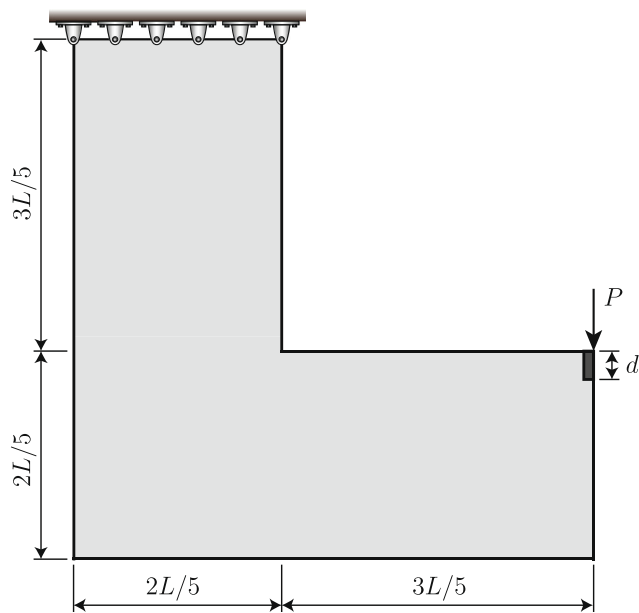


Fig. 5 Geometry and loading for the *L*-bracket problem

other regularization techniques that we investigated in the present study. In addition to the results reported in Table 3, Appendices C-G present a comprehensive analysis on the effects of the different components of the formulation in the quality of the optimization results. For instance, Appendix C investigates the effects of the stress constraint definition (i.e., the piecewise vanishing constraint) in the quality of the optimization results, while Appendices D-E study the effects of parameters  $\gamma_e$  and  $\eta$ , respectively. Appendix F demonstrates the benefits of restarting the AL parameters in terms of obtaining solutions of better quality (i.e., solutions with smaller mass ratio). Finally, Appendix G provides several numerical results for various values of the stress limit,  $\sigma_{lim}$ .

### 8.2.1 Effect of regularization techniques

Motivated by compliance minimization problems, different filtering techniques have been used in order to reduce

Table 2 Input parameters for the 2D *L*-bracket problem (Emmendoerfer and Fancello 2016)

Parameter	Description	Value
$E_0$	Young's modulus	1 Pa
$\nu$	Poisson's ratio	0.3
$\sigma_{lim}$	Stress limit	42 Pa
$L$	<i>L</i> -bracket length	1 m
$t$	Thickness	1 m
$P$	Applied load	1 N
$d$	Load distribution length	0.06 m
$r$	Filter radius	0.015 m

checkerboarding and mesh dependence (Bourdin 2001; Borrvall and Petersson 2001; Bendsøe and Sigmund 2003). Although these filtering techniques have also been used in stress-constrained topology optimization problems, their effect on this type of problems has, thus far, not been thoroughly studied. To illustrate the potentially adverse effect of using filters in stress-constrained topology optimization problems, we investigate a subset of the results displayed in Table 3.

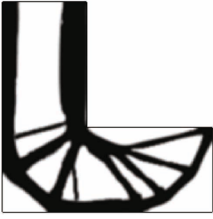
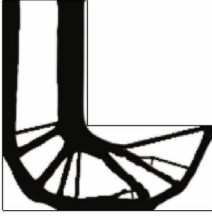
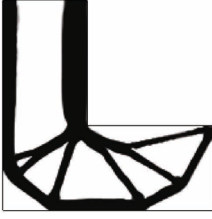
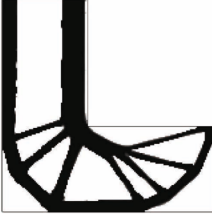
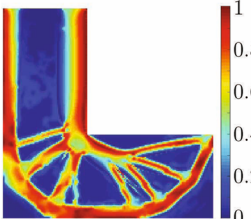
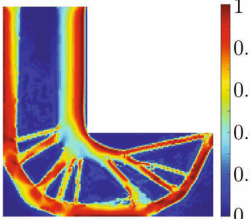
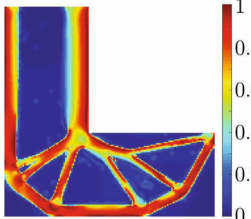
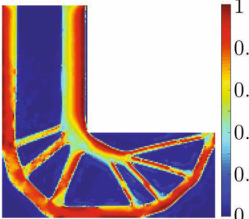
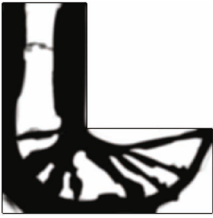
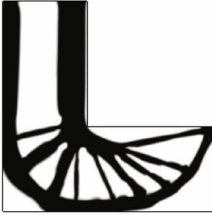
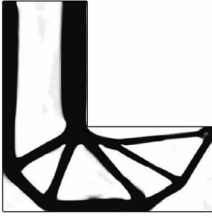
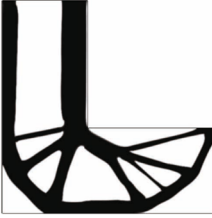
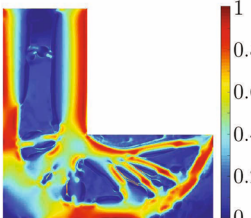
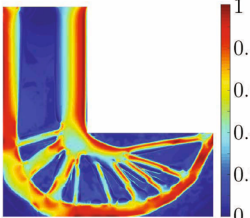
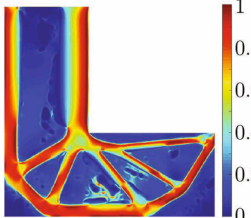
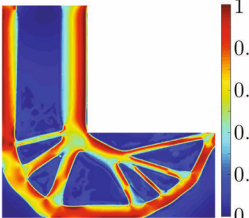
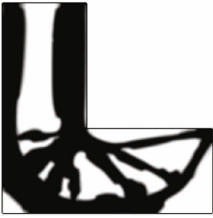
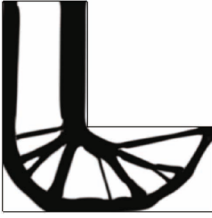
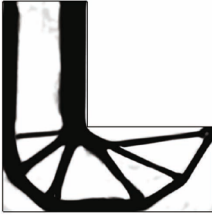
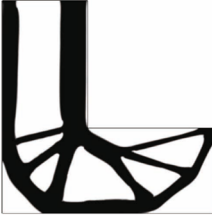
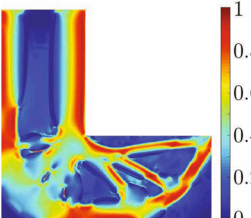
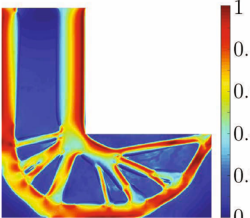
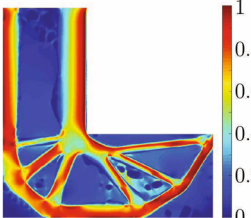
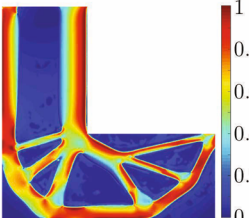
We focus on the *L*-bracket results for a 500,000 element mesh obtained using our filter reduction technique (see Table 3). Figure 6a shows both the topologies and normalized von Mises stress maps for an intermediate optimization step, before the filter reduction has been applied, and Fig. 6b shows these results at the end of the optimization iterations, when the filter reduction has been applied. Although the topologies before and after the filter reduction are nearly identical, the von Mises stress maps for these two density distributions are significantly different. We focus our attention around the highlighted regions on the right-hand side of Fig. 6a and b, in which the difference in von Mises stress is more prominent. Before the filter reduction is applied (Fig. 6a), this area exhibits a spike in the von Mises stress in a low density region. After the filter reduction is applied (Fig. 6b), the stress concentration in that void region is eliminated, leading to a well-defined von Mises stress map.

The spike in von Mises stress observed in Fig. 6a may be attributed to the diffuse interphasic regions between solid and void that are obtained after applying the filter to the density field. Because these diffuse interphasic regions have intermediate density, the apparent local von Mises stresses,  $\sigma_e^v$ , becomes considerably large (see Appendix B). This effect becomes more evident when dealing with fine meshes that have many elements in the interphasic regions, and it is primarily observed when the optimal design has sharp angles at corners and joints, as shown in the highlighted region of Fig. 6a.

In such cases, the use of a standard (e.g., linear) filter may prevent obtaining optimal designs with clear material boundaries. This observation suggests that stress-constrained topology optimization problems should be solved using filtering techniques that minimize the transition regions between solid and void.

We considered three approaches, as shown in the last three columns of Table 3, to reduce the interphasic regions between solid and void that appear as a result of density filters. Such approaches consists of using a polynomial filter, e.g., using  $s > 1$  in (15)<sub>2</sub>, the Heaviside projection (Guest et al. 2004), and our proposed filter reduction technique. However, other filtering schemes (e.g., see Wang and Wang 2005, 2011; Sigmund 2007; Xu et al. 2010; Talischi and Paulino 2013) that lead to a distinct boundary

**Table 3** Material distribution and relaxed von Mises stress for several regularization schemes and mesh sizes

Number of constraints	Linear filter	Polynomial filter ( $s = 3$ )	Heaviside	Filter reduction
16,380	 Volume = 45.7%	 Volume = 45.9%	 Volume = 40.3%	 Volume = 41.5%
				
160,000	 Volume = 61.0%	 Volume = 49.6%	 Volume = 42.6%	 Volume = 43.9%
				
500,000	 Volume = 60.4%	 Volume = 46.6%	 Volume = 44.5%	 Volume = 45.5%
				

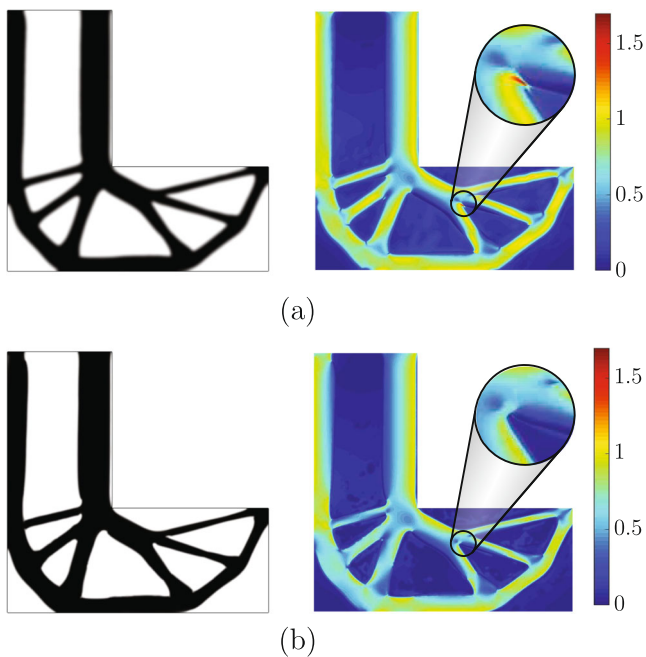


**Fig. 6** *L*-bracket results with a 500,000 element mesh. The optimized topologies (left) and normalized von Mises stress maps  $\tilde{\sigma}^v/\sigma_{lim}$  (right) are displayed for: **a** an intermediate optimization iteration, before filter reduction is used; and **b** the final solution, after filter reduction is applied

definition also have the potential to alleviate these spurious stress concentrations. For the sake of simplicity, in the remainder of this study, we combine a polynomial filter with exponent  $s \geq 1$  with a filter reduction technique to mitigate the adverse effect of the filter.

### 8.3 2D Wrench with multiple load cases

This example considers the design of a wrench domain subjected to stress constraints. The domain is discretized with PolyMesher (Talischì et al. 2012a) using 100,000 polygonal elements, and the finite element analysis routine is adopted from PolyTop (Talischì et al. 2012b). A description of the model geometry, loading conditions, and

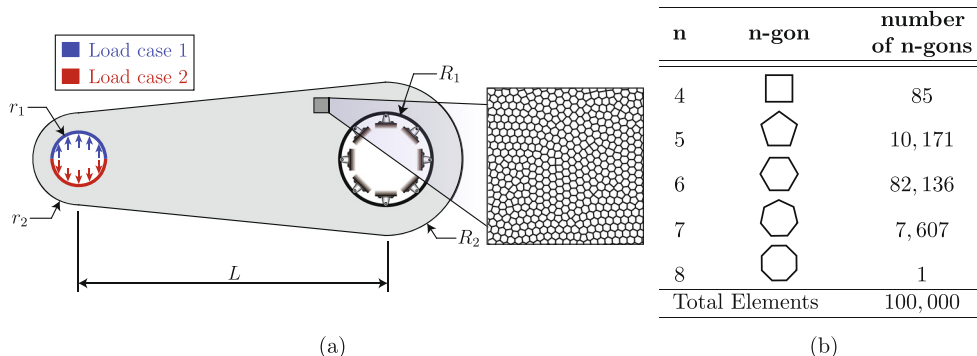
**Table 4** Input parameters for the wrench problem

Parameter	Description	Value
$E_0$	Young’s modulus	1 Pa
$\nu$	Poisson’s ratio	0.3
$\sigma_{lim}$	Stress limit	75 Pa
$L$	Wrench length	2 m
$t$	Thickness	1 m
$P$	Applied load	5.0 N
$r$	Filter radius	0.035 m

the composition of the polygonal mesh is provided in Fig. 7. To show how multiple load cases can be handled using our AL-based framework, we formulate the problem using two load cases, which in turn leads to symmetric topologies. The input parameters used to obtain the designs in the current example are displayed in Table 4. For this example, the geometry of the wrench is adopted from Talischì et al. (2012b), while the remaining parameters (e.g., loading and material parameters) are defined by the authors.

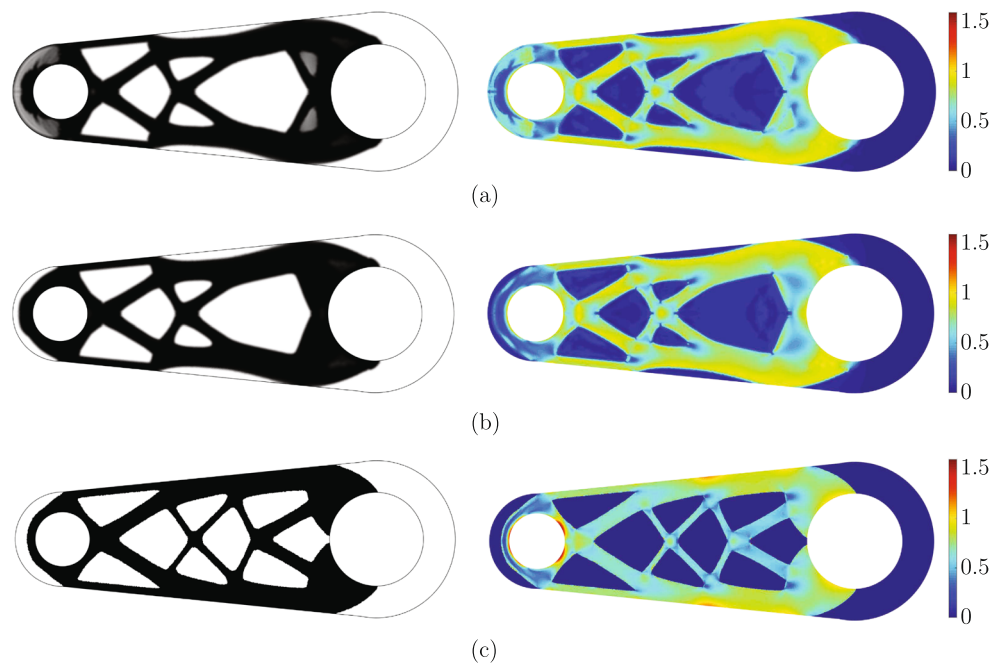
In order to handle multiple load cases, we impose  $N_e$  stress constraints per load case (i.e., one stress evaluation point per element and load case), which leads to  $N_c = mN_e$ , where  $m$  is the number of load cases. Because we consider two load cases for the wrench problem, we impose  $N_c = 2N_e$  stress constraints. To solve the stress-constrained problem, we add all  $N_c$  constraints to the penalty term of the AL function in Eq. (19). Adding more constraints instead of writing the optimization statement as a multi-objective topology optimization problem is possible because our objective function is the mass of the structure, which has no dependence on the number of load cases.

Figure 8 displays several optimized topologies for the wrench problem. The results in Fig. 8a correspond to those of the mass minimization problem with stress constraints when no Heaviside projection is used to compute the mass function (i.e., using  $\beta = 0$  in (16)). The results in Fig. 8b correspond to those obtained using a Heavisided density



**Fig. 7** Wrench problem set-up: **a** model geometry, loading, boundary conditions, and polygonal finite element discretization; and **b** composition of the FE mesh. The wrench domain is constructed using  $L = 2$  m,  $r_1 = 0.175$  m,  $r_2 = 0.3$  m,  $R_1 = 0.3$  m, and  $R_2 = 0.5$  m

**Fig. 8** Optimized topologies (left) and envelope of relaxed von Mises stress fields (right) for the wrench problem: **a** mass minimization problem with stress constraints without Heaviside projection of the mass objective function ( $\beta = 0$  in (16)); **b** mass minimization problem with stress constraints with Heaviside projection of the mass objective function ( $\beta = 3$  in (16)); **c** compliance minimization problem with 49% volume constraint. Unlike the compliance-based solution, the two stress-based solutions satisfy the stress limit at every evaluation point



field to compute the mass function (i.e., using  $\beta = 3$  in (16)). Finally, the results in Fig. 8c correspond to those obtained from a compliance minimization formulation with a volume constraint  $\bar{v} = 0.49$ , which corresponds to the optimized volume of the wrench of Fig. 8b.

The results show that the stress-based solution obtained for  $\beta = 0$  contains large regions of intermediate densities, while that for  $\beta = 3$  leads to a black-and-white design with clear material boundaries. This observation highlights the importance of using a density definition that disfavors intermediate densities during the optimization iterations. We also note that, although both the stress-based solution with  $\beta = 3$  and the compliance-based solution have the same volume fraction, i.e., 49%, the results from the mass minimization problem with stress constraints are significantly different from those for the compliance minimization problem with a volume constraint. The stress-constrained results drive the material away from the outer surfaces of the wrench, and the compliance minimization results drive the material towards the outer surfaces. By driving the material towards the outer surfaces of the wrench domain, the compliance minimization results violate the stress limit at several locations, as opposed to the stress-constrained results, which satisfy the stress limits in every evaluation point.

We also compare the compliance values obtained for both the stress-based solution and for the compliance-based solution. The compliance of the stress-based solution is 2,429 N-m, and that for the compliance-based solution is 2,098 N-m. Although the compliance of the stress-based

solution is 16% higher than that of the compliance-based solution, both are of the same order of magnitude. We expect to obtain similar values for the compliance of both formulations because the stress constraints limit the amount of local deformation of the final design, thus limiting the total compliance of the optimized solution.

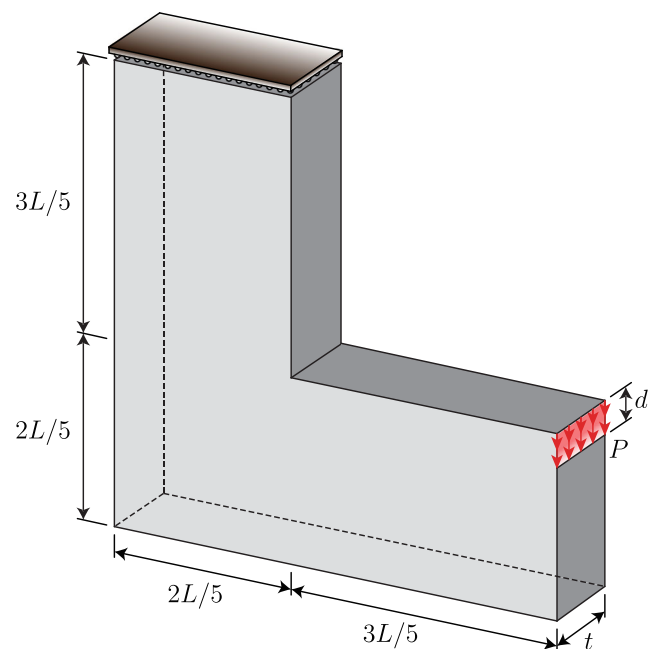
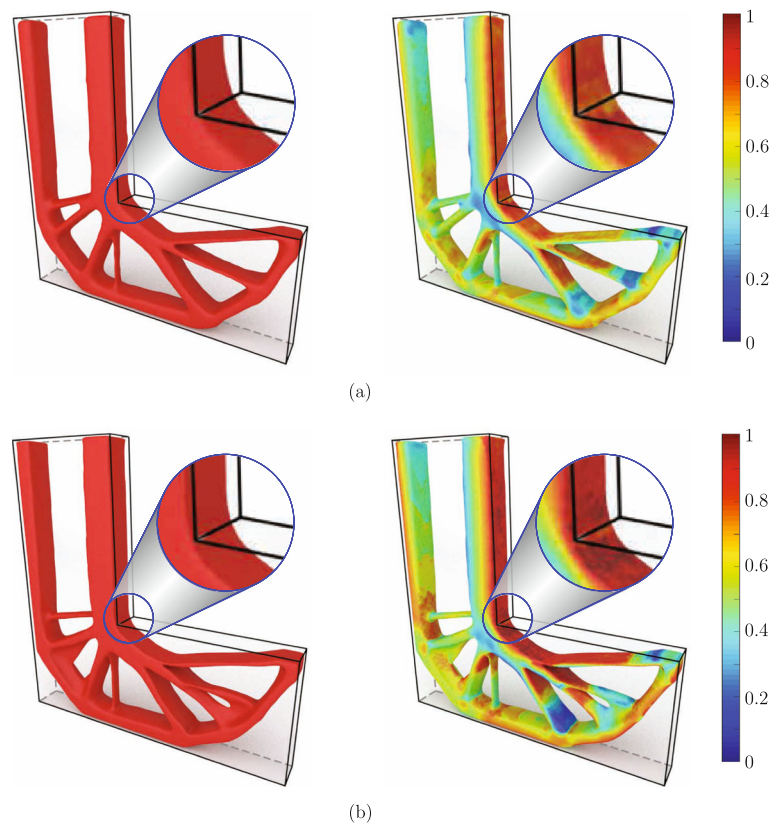


**Fig. 9** Geometry, loading, and boundary conditions for the 3D L-bracket

**Fig. 10** Optimized topologies (left) and normalized stress maps (right) obtained for the 3D *L*-bracket problem meshed with **a** 265,000 elements and **b** 1,728,000 elements. The topologies shown here correspond to the isosurface with cutoff value 0.5



The optimized topologies for the wrench depicted in Fig. 8 are symmetric, which is a direct result of using the two load cases shown in Fig. 7. Although a symmetric topology could have been enforced to the space of admissible density fields while using only one load case (e.g., see Talischi et al. 2012b), we considered two load cases to show how multiple load cases can be considered within the AL-based framework.

#### 8.4 3D *L*-bracket

In this example, we present the stress-constrained topology optimization results for a 3D *L*-bracket. The geometry of the 3D *L*-bracket is an extrusion of the 2D geometry from Section 8.2, as shown in Fig. 9. The applied load,  $P$ , is distributed uniformly across the thickness. For the results presented in this example, the geometry is discretized using regular hexahedral elements. In addition, two different meshes of increasing refinement are considered for the designs. The first mesh is composed of 265,000 elements and the second of 1,728,000 elements.

The input parameters for this example are adopted from those used in Table 2 for the 2D *L*-bracket example, except for the stress limit,  $\sigma_{\text{lim}} = 420$  Pa, and the thickness,  $t = 0.1$  m, which were adjusted accordingly.

Figure 10 shows the optimized topologies obtained for each of the two meshes considered in this example. As indicated in these results, our optimization methodology has successfully removed material from the reentrant corner of the *L*-bracket, thus removing the stress singularity at this location. The results displayed in Fig. 10 are based on STL files obtained from the isosurface representation of the optimized topologies.<sup>13</sup> Also, note that we obtain similar topologies with the two different discretizations.

The optimized topologies obtained for this example are similar to an extrusion of the topologies obtained for the 2D *L*-bracket example. That is because the thickness-to-length ratio for this problem is 1/10, i.e., it resembles a plane stress problem. The 3D topologies obtained in this example differ from those obtained by Sharma and Maute (2018) using the level-set method. In contrast with our optimized topologies, which are mainly composed of members with rectangular cross section, their optimized topologies are mainly composed of tubular members with approximately circular cross sections (i.e., their optimized topologies do

<sup>13</sup>The isosurfaces as well as the STL files are obtained using the MATLAB-based graphical tool TOPslicer (Zegard and Paulino 2016).

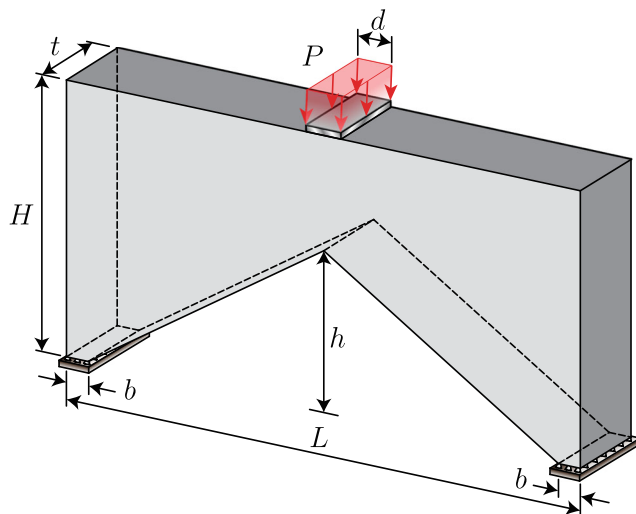


**Fig. 11** Geometry, loading, and boundary conditions for the 3D portal frame

not resemble an extrusion of a 2D topology). A possible reason to explain the difference between our results and those by Sharma and Maute (2018) is that they use the level-set method (favors curved boundaries) while we use a density-based method. We also note that their problem setting is different than the one used in this paper; while we aim to minimize the structural mass, they aim to minimize compliance plus a measure of the perimeter corresponding to the material domain boundary.

### 8.5 3D portal frame

This example presents the stress-constrained topology optimization results for the 3D portal frame depicted in Fig. 11. The material properties, dimensions, and loads for the 3D portal frame are shown in Table 5. These parameters

**Table 5** Input parameters for the 3D portal frame problem

Parameter	Description	Value
$E_0$	Young's modulus	$10^6$ Pa
$\nu$	Poisson's ratio	0.29
$\sigma_{\text{lim}}$	Stress limit	$1.5 \times 10^6$ Pa
$L$	Length	0.12 m
$H$	Height	0.06 m
$h$	Clear height	0.035 m
$b$	Bearing length	0.0055 m
$t$	Thickness	0.03 m
$P$	Applied load	120 N
$d$	Load distribution length	0.02 m
$r$	Filter radius	0.002 m

are adopted from a study by Le et al. (2010). Similarly to the  $L$ -bracket, the 3D portal frame analyzed in this example has a region of stress singularity at the reentrant corner located on the lower portion of the portal midspan.

Figures 12 and 13 depict the optimization results obtained for a mesh with 633,240 elements and 1,236,300 elements, respectively. These results are obtained in a similar way as those in the previous example. As observed from these results, our AL-based topology optimization formulation is able to remove material from the reentrant corner, thus preventing stress singularities and satisfying the stress constraints at every evaluation point. Moreover, the structures in Figs. 12 and 13 present similar geometries.

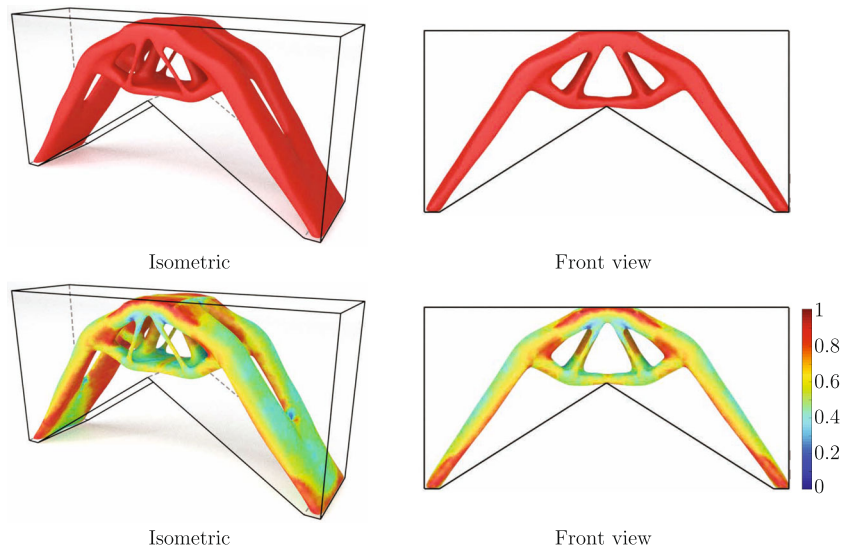
## 9 Assessment of computational efficiency

The stress-constrained problem is often associated with a high computational cost. This section evaluates the efficiency of the AL-based topology optimization methodology presented in Section 5 by analyzing the computational cost of the different examples presented in the previous section.<sup>14</sup> In general, the bottleneck of the implementation is the solution of the linear systems  $\mathbf{K}(\mathbf{z})\mathbf{u} = \mathbf{f}$  (equilibrium equation) and  $\mathbf{K}(\mathbf{z})\boldsymbol{\xi} = \tilde{\mathbf{f}}$  (adjoint problem) at each optimization step. For the 2D cases, the linear systems are solved using the Cholesky decomposition of the stiffness matrix. The Cholesky decomposition is stored and used to find both displacement vector  $\mathbf{u}$  and adjoint vector  $\boldsymbol{\xi}$  via backward and forward substitution. For the 3D cases, the resulting stiffness matrix is considerably less sparse. Therefore, the linear systems are solved via an iterative solver using MATLAB's GPU implementation of the preconditioned conjugated gradient with the Jacobi preconditioner.

The computational cost obtained for all examples in the previous section are shown in Table 6. The results for the 2D  $L$ -bracket show the number of iterations required by the filter reduction scheme is smaller than that required for all other regularization techniques. We also observe that, for all mesh sizes, the filter reduction technique led to the smallest computational cost when compared to the other regularization techniques. For the 16,380 element mesh, the Heaviside projection method was the slowest among all the other regularization techniques; however, for the 160,000 and 500,000 element mesh, the linear filter was the slowest, followed by the Heaviside projection method.

<sup>14</sup>The computational costs reported in this section are based on the topology optimization results obtained in a computer with an i7-4930k CPU at 3.40 GHz and 64 GB of RAM and a NVIDIA GEFORCE GTX 1080 Ti GPU running on a 64-bit operating system.

**Fig. 12** Optimized topology (top) and normalized stress map (bottom) obtained for the 3D portal frame problem meshed with 633,240 elements (633,240 stress constraints). The topologies shown here correspond to the isosurface with cutoff value 0.5



The computational time for the 2D wrench problem is slightly larger than that of other problems with a similar mesh size. That is because the wrench domain was discretized using polygonal elements, in which the FE model has more degrees of freedom for the same number of design variables, and also because the wrench problem is defined using two load cases.

We also observe a large discrepancy between the performances of the 2D and the 3D models, which is due to the larger and less sparse linear systems  $\mathbf{K}(\mathbf{z})\mathbf{u} = \mathbf{f}$  associated with 3D models. We also observed that computational time for the coarser 3D portal frame, which is discretized with 633,240 elements, is nearly one half

of that for the coarser 3D *L*-bracket, which is discretized with 265,200 elements. This observation prompted an investigation to identify the source of this apparent inconsistency. To find the source of this discrepancy, we analyzed the number of iterations required by the preconditioned conjugate gradient (PCG) solver to solve the linear systems,  $\mathbf{K}(\mathbf{z})\mathbf{u} = \mathbf{f}$ , at every optimization step. The results from this analysis showed that, on average, the number of PCG iterations required for the 3D *L*-bracket was much larger than that required for the 3D portal frame, which considerably increases the computational cost for the 3D *L*-bracket, and as a result, explains the observed discrepancy.

**Fig. 13** Optimized topology (top) and normalized stress map (bottom) obtained for the 3D portal frame problem meshed with 1,236,375 elements (1,236,375 stress constraints). The topologies shown here correspond to the isosurface with cutoff value 0.5

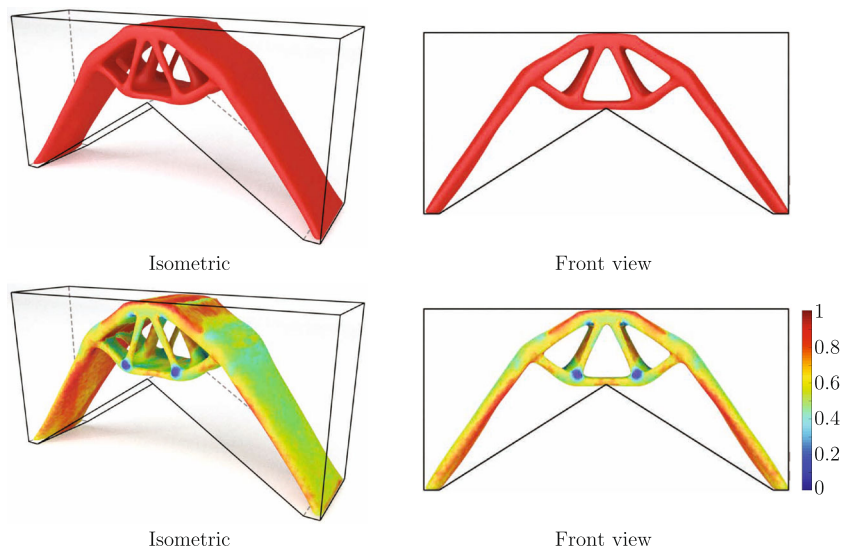


**Table 6** Computational cost for the different numerical examples

Problem	Mesh	Regularization	Iteration <sup>†</sup>	Time
2D <i>L</i> -bracket	16,380	Linear filter	788	3.4 min
	16,380	Polynomial filter	943	4.5 min
	16,380	Heaviside projection	1440	6.2 min
	16,380	Filter reduction	524	2.5 min
	160,000	Linear filter	2131	208.3 min
	160,000	Polynomial filter	1239	65.5 min
	160,000	Heaviside projection	1466	75.2 min
	160,000	Filter reduction	590	36.5 min
	500,000	Linear filter	1571	6.5 h
	500,000	Polynomial filter	1028	3.8 h
2D wrench	100,000	Filter reduction	807	1.1 h
	265,200	Filter reduction	480	12.2 h
3D <i>L</i> -bracket	1,728,000	Filter reduction	520	97.8 h
	633,240	Filter reduction	303	7.1 h
3D portal frame	1,236,375	Filter reduction	466	34.4 h

<sup>†</sup> The iterations reported here correspond to the number of times the MMA optimizer is called and not to the number of AL steps,  $k$

## 10 Concluding remarks

This paper emphasizes on *consistency* between topology optimization considering stress constraints and continuum mechanics. Thus, we present a topology optimization formulation for mass minimization with local stress constraints, which is *consistent* with continuum mechanics in the sense that stresses are treated locally (Cauchy 1827), i.e., neither aggregated nor clustered.<sup>15</sup>

Specifically, we present a methodology for topology optimization with local stress constraints based on the augmented Lagrangian (AL) method. We introduce two modifications to the AL function, which are tailored to solve mass minimization problems with stress constraints. The first modification, involving a scale factor  $\eta$ , is introduced to normalize the penalization term of the AL function with respect to the number of constraints, which leads to a stable method as the mesh is refined or coarsened. The second modification, involving the weight factors  $\gamma_e$ , is introduced in order to improve convergence to a black-and-white (0/1) solution and to overcome local optima with high volume. The weight factors are adaptively adjusted during the optimization process with a heuristic rule.

We introduce a modified version of the vanishing constraint, denoted as *piecewise vanishing constraint*. The modified vanishing constraint, together with the

modifications to the AL function, lead to a stable formulation that is capable of solving a wide range of two- and three-dimensional topology optimization problems for a wide range of mesh sizes, without adjusting the algorithmic parameters. We conduct extensive numerical studies that support our rationale for the aforementioned modifications and show that the results, obtained when the modifications are included, are of better quality than those obtained when they are not considered. The formulation treats stress as a local quantity, satisfying every local stress constraint, and it is able to do so in a computationally efficient fashion.

Another finding from this work relates to the use of regularization techniques in stress-constrained topology optimization problems. Our results indicate that the use of a linear filter may hinder the optimizer from achieving meaningful solutions because the von Mises stress fields are highly affected by the presence of interphases of intermediate densities between solid and void material, particularly when the optimized structures have sharp angles at joints and corners and when the domain is discretized with a relatively fine mesh. As a result, stress-constrained topology optimization problems should be solved using techniques to minimize the intermediate densities of the solid/void interface. We employ a continuation technique on the filter radius that alleviates this problem and provides clear material boundaries. We acknowledge that other approaches can be used to mitigate this issue (e.g., projection schemes that decrease the amount of intermediate densities). However, for the problems solved and the approaches implemented in this study, the proposed filter reduction scheme yields satisfactory results.

<sup>15</sup>On the other hand, an inconsistent formulation refers to the case in which stresses are not treated locally, i.e., they are either aggregated or clustered.

**Acknowledgments** This paper is dedicated to the memory of Augustin-Louis Cauchy (August 21, 1789 - May 23, 1857). We thank Mrs. Emily D. Sanders for useful suggestions that contributed to improve the manuscript.

**Funding information** F.V.S., O.G.-L., and G.H.P. acknowledge the financial support from the US National Science Foundation under grant #1663244 and the endowment provided by the Raymond Allen Jones Chair at the Georgia Institute of Technology. F.V.S. and I.F.M.M. acknowledge the support provided by Brazilian agencies CNPQ and FAPERJ, and Tecgraf/PUC-Rio (Group of Technology in Computer Graphics), Rio de Janeiro, Brazil.

**Compliance with ethical standards**

**Conflict of interest** The authors declare that they have no conflict of interest.

**Replication of results** The paper includes details of the numerical implementation and all input parameters for the numerical examples are provided to facilitate replication of the results. To help with the dissemination of the original ideas presented here, we follow-up with the publication of an educational paper and corresponding Matlab code for stress constrained topology optimization in the SMO Journal (Giraldo-Londoño and Paulino 2020).

**Appendix A: Augmented Lagrangian method for inequality constraints**

The procedure described in Section 4 is designed to solve optimization problems with equality constraints. For the sake of completeness, and to provide the reader interested in applying the AL method to problems with inequality constraints, we present an extension of the AL method for inequality constraints. As usual, we handle inequality constraints by introducing slack variables  $s_j$ ,  $j = 1, \dots, N_c$  to the optimization problem (Nocedal and Wright 2006). Consider the following optimization problem with inequality constraints:

$$\begin{aligned} \min_{\mathbf{z} \in \mathbb{R}^n} \quad & f(\mathbf{z}) \\ \text{s.t.} \quad & g_j(\mathbf{z}) \leq 0 \quad \forall j = 1, \dots, N_c \\ & \mathbf{L} \leq \mathbf{z} \leq \mathbf{U}, \end{aligned} \tag{37}$$

where  $\mathbf{L}$  and  $\mathbf{U}$  define the lower and upper bounds of the design variables, respectively. Introducing slack variables, constraints  $g_j(\mathbf{z}) \leq 0$  are rewritten as follows:

$$h_j(\mathbf{z}) = g_j(\mathbf{z}) + s_j = 0, \quad s_j \geq 0, \quad j = 1, \dots, N_c. \tag{38}$$

Consequently, the approximate sub-problem that needs to be solved at the  $k$ th step of the AL method is as follows:

$$\begin{aligned} \min_{\mathbf{z}, \mathbf{s}} \quad & J^{(k)}(\mathbf{z}, \mathbf{s}) = f(\mathbf{z}) + \sum_{j=1}^{N_c} \left[ \lambda_j^{(k)} (g_j(\mathbf{z}) + s_j) + \frac{\mu^{(k)}}{2} (g_j(\mathbf{z}) + s_j)^2 \right] \\ \text{s.t.} \quad & \mathbf{L} \leq \mathbf{z} \leq \mathbf{U} \\ & s_j \geq 0 \quad \forall j = 1, \dots, N_c. \end{aligned} \tag{39}$$

The minimization of  $J^{(k)}(\mathbf{z}, \mathbf{s})$  with respect to the slack variables is obtained explicitly for any fixed  $\mathbf{z}$  by solving the optimization problem as follows:

$$\begin{aligned} \min_{s_j} \quad & \left[ \lambda_j^{(k)} (g_j(\mathbf{z}) + s_j) + \frac{\mu^{(k)}}{2} (g_j(\mathbf{z}) + s_j)^2 \right] \\ \text{s.t.} \quad & s_j \geq 0. \end{aligned} \tag{40}$$

The optimization statement (40) is defined in terms of the slack variable,  $s_j$ , associated with constraint  $g_j$ . As a result, its solution can be found in closed form using the stationary conditions of the Lagrangian of Eq. (40), which leads to the following:

$$s_j = \max \left[ 0, - \left( \frac{\lambda_j^{(k)}}{\mu^{(k)}} + g_j(\mathbf{z}) \right) \right] \quad \forall j = 1, \dots, N_c. \tag{41}$$

Substituting (41) into (38) leads to the following:

$$h_j(\mathbf{z}) = \max \left[ g_j(\mathbf{z}), - \frac{\lambda_j^{(k)}}{\mu^{(k)}} \right] \quad \forall j = 1, \dots, N_c. \tag{42}$$

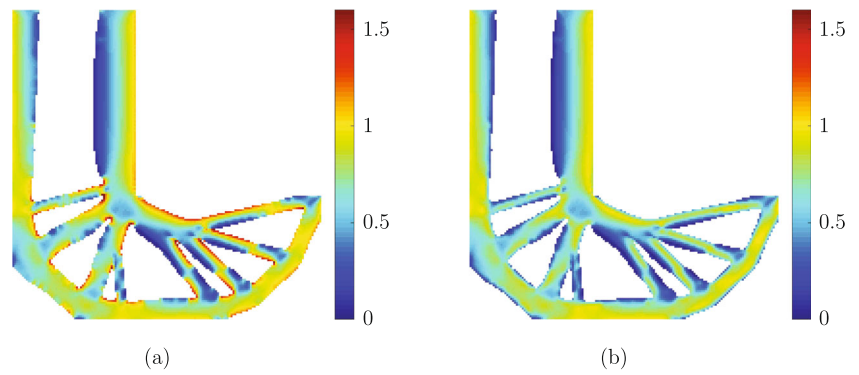
Using (42), the inequality constraints  $g_j(\mathbf{z}) \leq 0$  of (37) can be replaced by equality constraints, allowing the problem to be solved using the procedure described for solving the equality-constrained problem (6). As inferred from (42), the slack variables do not need to be computed explicitly, facilitating the implementation of the AL method with inequality constraints. One must recall that the Lagrange multiplier estimators,  $\lambda_j^{(k)}$ , and the penalty factor,  $\mu^{(k)}$ , remain constant for each AL sub-problem, and thus the AL function is continuously differentiable (with respect to the design variables) at each AL step. Despite the presence of the maximum function, the AL function used with (42) is differentiable even at the points in which  $g_j(\mathbf{z}) = -\lambda_j^{(k)}/\mu^{(k)}$ .<sup>16</sup> If (17) is substituted into (42), it follows that  $g_j(\mathbf{z}) = h_j(\mathbf{z})$ , which is the case in our implementation of the AL-based method. However, if one were to use a different stress constraint definition that can take negative values, then (42) (in its explicit form) would be necessary in the implementation.

**Appendix B: Apparent “local” von Mises stress vs. stress measure**

Here, we clarify the difference between the apparent “local” von Mises stress,  $\sigma^v$ , and the stress measure,  $\tilde{\sigma}^v$ , described in Section 5.2. Using a stress measure of the form  $\tilde{\sigma}^v = \rho^\alpha \sigma^v$  is a typical procedure in the context of stress-based topology optimization (e.g., Bruggi and Duysinx 2012; Lee et al. 2012), because the apparent “local” von Mises stress

<sup>16</sup>The interested reader is referred to Bertsekas (1996, p. 161) for complete proof of the differentiability of the AL function used with (42).

**Fig. 14** Normalized apparent “local” von Mises stress **a** and normalized stress measure **b** for the 16,380 mesh solution with linear filter of the *L*-bracket example in Table 3. The stress is only displayed for the regions with density above 0.05. Because both stresses are normalized, the value of 1 represents the stress limit



is large in regions of low density. The high stresses in regions of low density can be seen in Fig. 14a (only regions with density above 0.05 are shown), which displays the normalized apparent “local” von Mises stress for the 16,380 mesh solution with linear filter of the *L*-bracket example in Table 3. We observe that the largest apparent local stress occurs at the boundaries between solid and void, in which the density is small due to the filter operator. In contrast, Fig. 14b shows the normalized stress measure of the same solution, in which the stress measure strictly satisfies the stress limit of 1. By adopting  $\tilde{\sigma}^v = \rho^{0.5}\sigma^v$ , we reduce the effect of the vaguely defined stress in the regions of low density.

**Appendix C: Comparison of the piecewise vanishing constraint with  $\epsilon$ -relaxation**

We compare the optimization results obtained using our piecewise vanishing constraint with those obtained using

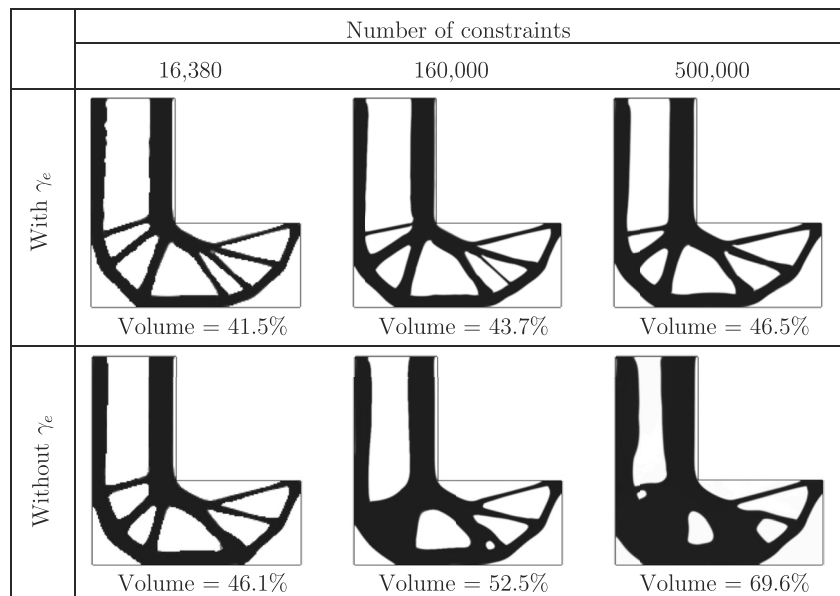
the  $\epsilon$ -relaxed constraint (Cheng and Guo 1997). The  $\epsilon$ -relaxation approach used here is the one proposed by Cheng and Guo (1997) and Petersson (2001) in which we start with a value of  $\epsilon = 0.01$ , and we set the lower bound of the design variable to  $\epsilon^2$ . The value of  $\epsilon$  is divided by two every time that we restart the AL parameters to gradually decrease the value of  $\epsilon$  reaching a final value of  $\epsilon = 0.000625$ . We also update the lower bound of the design variable so that it is always equal to  $\epsilon^2$ .

Figure 15 displays the results that we obtain using each of these constraints. As compared to the designs obtained using the piecewise vanishing constraint, those obtained using the  $\epsilon$ -relaxed constraint have a significantly larger volume and contain regions of pure solid material (which appear sub-optimal) near the bottom left corner of the bracket. Based on the information displayed on Fig. 15, the results obtained using the piecewise vanishing constraint outperform those obtained using  $\epsilon$ -relaxation constraint in terms of both optimized volume and quality of results.

**Fig. 15** Optimized topologies for an *L*-bracket obtained using the piecewise vanishing constraint (top) and using the  $\epsilon$ -relaxed constraint (bottom)

	Number of constraints		
	16,380	160,000	500,000
Piecewise vanishing constraint	 Volume = 41.5%	 Volume = 43.7%	 Volume = 46.5%
$\epsilon$ -relaxed constraint	 Volume = 52.2%	 Volume = 55.7%	 Volume = 59.2%

**Fig. 16** Optimized topologies for an *L*-bracket obtained when weight factors  $\gamma_e$  are considered (top) and when they are not considered (bottom)



**Appendix D: Effect of weight factors  $\gamma_e$**

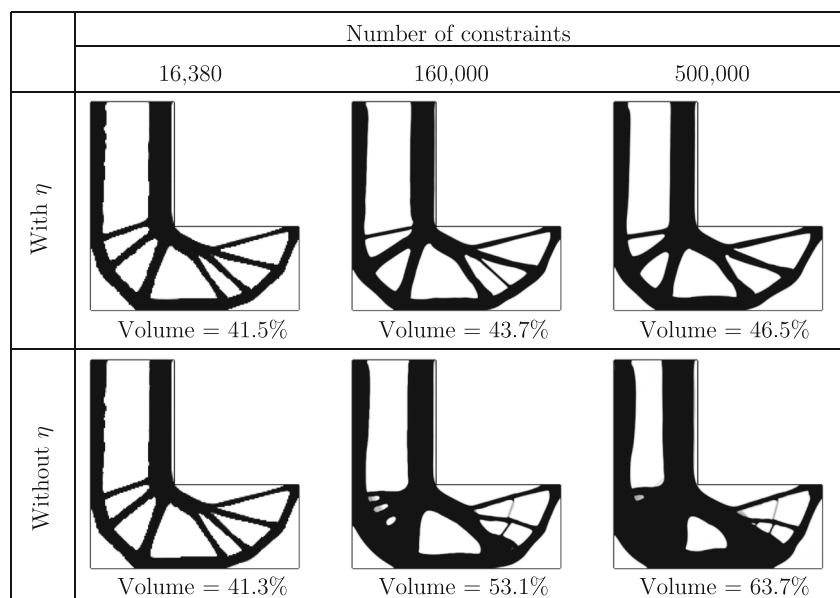
The introduction of weight factors  $\gamma_e$  is one of the main characteristics of the present formulation. Here, we investigate the effects of using the weight factors in the optimization results obtained for the *L*-bracket. Figure 16 presents the results that we obtain using  $\gamma_e$ , as well as, those not using  $\gamma_e$ . We observe that, as compared to the results obtained with  $\gamma_e$ , those obtained without  $\gamma_e$  have a higher final volume and have fewer beam-like elements. The factor  $\gamma_e$  helps the optimizer to overcome unfavorable local optima by increasing the relevance of the objective function in elements which have low stress value. If  $\gamma_e$  is not considered, the optimizer is likely to get trapped in a

bad local optima with high volume, preventing it to achieve structures with more slender elements, as we expect for this benchmark problem.

**Appendix E: Effect of scale factor  $\eta$**

The scale factor,  $\eta$ , is introduced to normalize the values of the AL penalization parameters,  $\mu^{(k)}$  and  $\lambda_j^{(k)}$ , such that we eliminate the need for adjusting the numerical values of  $\mu^{(1)}$  and  $\lambda_j^{(1)}$  for problems with different number of constraints. We demonstrate the effectiveness of the parameter  $\eta$  through the numerical results shown in Fig. 17. These results correspond to the optimized topologies obtained for the

**Fig. 17** Optimized topologies for an *L*-bracket obtained when scale factor  $\eta$  is considered (top) and when it is not considered (bottom)



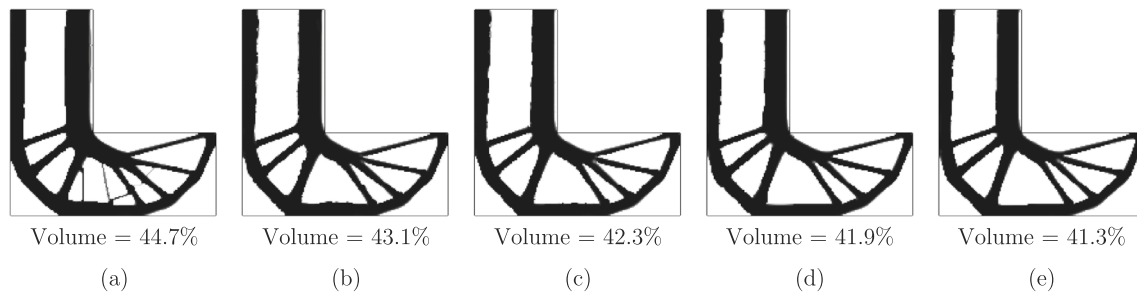


**Fig. 18** Effect of the number of AL parameter restarts on the optimized topologies obtained for an  $L$ -bracket meshed with 16,380 elements: **a** no restart; **b** one restart; **c** two restarts; **d** three restarts;

and **e** four restarts. As the number of restarts increases, the small-scale artifacts are removed and the optimized volume fraction becomes smaller

$L$ -bracket when the parameter  $\eta$  is either used or not. For the case when the parameter  $\eta$  is not used, we re-calibrate the values of  $\mu^{(1)}$  and  $\lambda_j^{(1)}$  for a mesh size of 16,380 elements, and these values are used to obtain the optimized topologies for the other mesh sizes. As the mesh is refined (i.e., as the number of constraints increases), the results obtained when  $\eta$  is not used are clearly worse than those obtained when  $\eta$  is used. That is because when  $\eta$  is not considered, the magnitude of the penalty parameter of the AL function (19) increases as the number of constraints increases. Without the  $\eta$  parameter to normalize this effect, the optimizer becomes trapped in local optima with higher volume.

### Appendix F: Effect of the number of AL parameter restarts

We investigate the effect of restarting the AL parameters,  $\lambda_j^{(k)}$  and  $\mu^{(k)}$ , as well as the weight factors,  $\gamma_e^{(k)}$ , on the final solution (cf. Section 7.1). As illustrated by Fig. 18, restarting these parameters helps us achieve a solution with overall lower volume. The results presented in the figure correspond to the final solutions of the  $L$ -bracket problem with 16,380 elements that we obtained using the filter reduction approach for various numbers of restarts.

As shown by the results in Fig. 18, the topology obtained with no restart contains several small-scale artifacts, which cannot be removed without increasing the stress in the structure. As a result, the solution gets trapped in an unfavorable local optimum with higher volume. After the first restart, the small-scale features disappear and the final volume becomes smaller. If we keep restarting the AL parameters and weight factors when the optimization stagnates, the total volume that we are able to reach keeps decreasing because the optimizer is able to find local optima with lower volume.

### Appendix G: Effect of stress limit $\sigma_{lim}$

We analyze the effect of the stress limit,  $\sigma_{lim}$ , in the optimization results obtained for the  $L$ -bracket with 16,380 elements. The optimization results obtained using our AL-based framework with the filter reduction scheme are depicted in Fig. 19. The results demonstrate that increasing the stress limit leads to designs with lower volume fraction and more slender members, yet all these designs are topologically similar. A more significant change of topology is observed when  $\sigma_{lim} \geq 80$  Pa, in which the vertical member of the left edge of the  $L$ -bracket begins to tilt. The results also demonstrate that the optimized volume decreases monotonically as we increase the stress limit. Although not shown in the figure, our numerical results also indicate that the minimum stress limit possible for this optimization problem is around 37 Pa. That is because the final volume obtained from the optimization results increase significantly as the stress limit approaches this value.

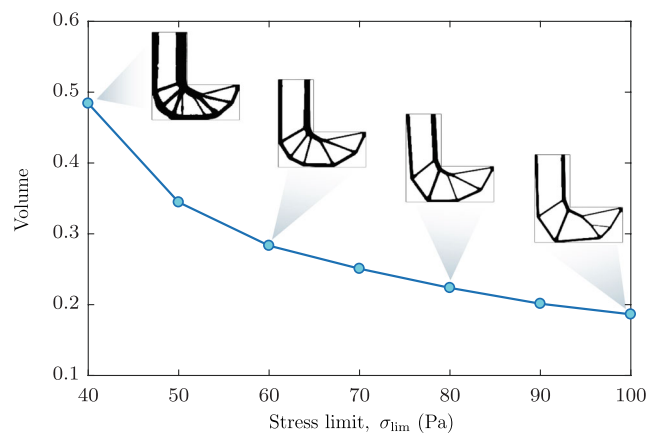


**Fig. 19** Optimized volume of the  $L$ -bracket meshed with 16,380 elements as a function of the stress limit

## Appendix H: Nomenclature

$\alpha$	Parameter used to update penalty parameter $\mu^{(k)}$
$\lambda^{(k)}$	Vector of approximated Lagrange multipliers at the $k$ th iteration of the AL method
$\xi$	Adjoint vector used for sensitivity evaluation
$\eta$	Scale factor used in the AL function (19)
$\gamma_L, \gamma_U$	Lower and upper bounds of weight factors $\gamma_e$ , respectively
$\gamma_e$	Weight factor for element $e$ used in the modified AL function (19)
$\mu^{(k)}$	Penalty parameter at the $k$ th iteration of the AL method
$\nu$	Poisson's ratio of solid material
$\sigma_e^v$	von Mises stress at the centroid of element $e$
$\sigma_{\text{lim}}$	Stress limit for a given material
$\epsilon$	Ersatz stiffness
$\varepsilon$	Relaxation parameter in $\varepsilon$ -relaxed approach
$\rho$	Vector of filtered densities
$\tilde{\rho}_e$	Volume fraction of element $e$ , defined using a smooth Heaviside projection function
$\Delta$	Infinitesimal quantity
$E_0$	Young's modulus of solid material
$J^{(k)}(\mathbf{z})$	Augmented Lagrangian function at iteration $k$
$N_c$	Number of stress constraints
$N_e$	Number of elements in a finite element mesh
$\beta$	Mass penalization parameter used in the smooth Heaviside projection function
<b>K</b>	Global stiffness matrix
<b>P</b>	Filter matrix
<b>f</b>	Global force vector
<b>k<sub>e</sub></b>	Element stiffness matrix
<b>s</b>	Vector of slack variables
<b>u</b>	Global displacement vector
<b>z</b>	Vector of design variables
$a_i, b_i$	Parameters used to define the evolution of weight factors $\gamma_e$ ( $i = 1, 2$ )
$f$	Objective function
$g_j(\mathbf{z})$	$j$ th stress constraint
$h$	Equality constraint
$h_j(\mathbf{z})$	$j$ th modified stress constraint used in the AL method with inequality constraints
$m(\mathbf{z})$	Mass of the structure
$p$	Stiffness penalization parameter
$q$	Relaxation parameter in qp-relaxed approach
$r$	Filter radius
$s$	Exponent of the polynomial filter
$v_e$	Volume of element $e$ for density equal one

## References

- Achtziger W, Kanzow C (2008) Mathematical programs with vanishing constraints: optimality conditions and constraint qualifications. *Math Program* 114(1):69–99

- Achtziger W, Hoheisel T, Kanzow C (2013) A smoothing-regularization approach to mathematical programs with vanishing constraints. *Comput Optim Appl* 55(3):733–767
- Amstutz S, Novotny AA (2010) Topological optimization of structures subject to von Mises stress constraints. *Struct Multidiscip Optim* 41(3):407–420
- Andreani R, Haeser G, Schuverdt M, Silva P (2012) A relaxed constant positive linear dependence constraint qualification and applications. *Math Program* 135(1-2):255–273
- Bell E. T. (1986) *Men of Mathematics*. Simon and Schuster
- Bendsøe MP (1989) Optimal shape design as a material distribution problem. *Struct Optim* 1:193–202
- Bendsøe MP, Kikuchi N (1988) Generating optimal topologies in structural design using a homogenization method. *Comput Methods Appl Mech Eng* 71(2):197–224
- Bendsøe MP (1995) *Optimization of structural topology, shape, and material*. Springer, Berlin
- Bendsøe MP, Sigmund O (1999) Material interpolation schemes in topology optimization. *Arch Appl Mech* 69(9-10):635–654
- Bendsøe MP, Sigmund O (2003) *Topology optimization: theory, methods and applications*. Springer, Berlin
- Bertsekas DP (1996) *Constrained optimization and Lagrange multiplier methods (optimization and Neural Computation Series)*, 1 ed. Athena Scientific
- Bertsekas DP (1999) *Nonlinear programming*, 2nd ed. Athena Scientific
- Borrvall T, Petersson J (2001) Topology optimization using regularized intermediate density control. *Comput Methods Appl Mech Eng* 190(37-38):4911–4928
- Bourdin B (2001) Filters in topology optimization. *Int J Numer Methods Eng* 50(9):2143–2158
- Bruggi M (2008) On an alternative approach to stress constraints relaxation in topology optimization. *Struct Multidiscip Optim* 36(2):125–141
- Bruggi M, Duysinx P (2012) Topology optimization for minimum weight with compliance and stress constraints. *Struct Multidiscip Optim* 46(3):369–384
- Cauchy AL (1827) De la pression ou tension dans un corps solide. *Exercices Math* 2:42–56
- Cheng G, Jiang Z (1992) Study on topology optimization with stress constraints. *Eng Optim* 20(2):129–148
- Cheng G (1995) Some aspects on truss topology optimization. *Struct Optim* 10(3-4):173–179
- Cheng G, Guo X (1997)  $\varepsilon$ -relaxed approach in structural topology optimization. *Struct Optim* 13(4):258–266
- Christensen P, Klarbring A (2008) *An introduction to structural optimization. Solid Mechanics and Its Applications*. Springer, Netherlands
- da Silva GA, Beck AT, Sigmund O (2019) Stress-constrained topology optimization considering uniform manufacturing uncertainties. *Comput Methods Appl Mech Eng* 344:512–537
- Duysinx P, Bendsøe MP (1998a) Topology optimization of continuum structures with local stress constraints. *Int J Numer Methods Eng* 43(8):1453–1478
- Duysinx P, Sigmund O (1998b) New developments in handling stress constraints in optimal material distribution. In: *Proceedings of the 7th AIAA/USAF/NASA/ISSMO Symposium on Multidisciplinary Analysis and Optimization*, vol 1, pp 1501–1509
- Emmendoerfer Jr, H, Fancello EA (2014) A level set approach for topology optimization with local stress constraints. *Int J Numer Methods Eng* 99(2):129–156
- Emmendoerfer Jr, H, Fancello EA (2016) Topology optimization with local stress constraint based on level set evolution via reaction-diffusion. *Comput Methods Appl Mech Eng* 305:62–88
- Ermoliev YM, Kryazhinskii AV, Ruzschiński A (1997) Constraint aggregation principle in convex optimization. *Math Program* 76(3):353–372

- Gibson I, Rosen D, Stucker B (2015) Additive manufacturing technologies: 3D printing, rapid prototyping, and direct digital manufacturing, vol 2. Springer, Berlin
- Giraldo-Londoño O, Paulino GH (2020) PolyStress: a Matlab implementation for local stress-constrained topology optimization considering material nonlinearity. *Struct Multidiscip Optim*. <https://doi.org/10.1007/s00158-020-02664-7>
- Guest JK, Prévost JH, Belytschko T (2004) Achieving minimum length scale in topology optimization using nodal design variables and projection functions. *Int J Numer Methods Eng* 61(2):238–254
- Guo X, Zhang WS, Wang MY, Wei P (2011) Stress-related topology optimization via level set approach. *Comput Methods Appl Mech Eng* 200(47–48):3439–3452
- Gurtin ME (1981) An introduction to continuum mechanics, vol 158. Academic Press
- Hoheisel T, Kanzow C (2008) Stationary conditions for mathematical programs with vanishing constraints using weak constraint qualifications. *J Math Anal Appl* 337(1):292–310
- Holmberg E, Torstenfelt B, Klarbring A (2013) Stress constrained topology optimization. *Struct Multidiscip Optim* 48(1):33–47
- Izmailov AF, Solodov MV, Uskov EI (2012) Global convergence of augmented lagrangian methods applied to optimization problems with degenerate constraints, including problems with complementarity constraints. *SIAM J Optim* 22(4):1579–1606
- James K, Lee E, Martins J (2012) Stress-based topology optimization using an isoparametric level set method. *Finite Elem Anal Des* 58:20–30
- Kirsch U (1989) Optimal topologies in truss structures. *Comput Methods Appl Mech Eng* 72(1):15–28
- Kirsch U, Taye S (1986) On optimal topology of grillage structures. *Eng Comput* 1:229–243
- Kirsch U (1990) On singular topologies in optimum structural design. *Struct Optim* 2(3):133–142
- Kiyono C, Vatanabe S, Silva E, Reddy J (2016) A new multi-p-norm formulation approach for stress-based topology optimization design. *Compos Struct* 156:10–19. 70th Anniversary of Professor J. N. Reddy
- Kreisselmeier G, Steinhauser R (1979) Systematic control design by optimizing a vector performance index. *IFAC Proc Vol* 12(7):113–117. IFAC Symposium on computer Aided Design of Control Systems, Zurich, Switzerland
- Le C, Norato J, Bruns T, Ha C, Tortorelli D (2010) Stress-based topology optimization for continua. *Struct Multidiscip Optim* 41(4):605–620
- Lee E, James KA, Martins JRRA (2012) Stress-constrained topology optimization with design-dependent loading. *Struct Multidiscip Optim* 46(5):647–661
- Lian H, Christiansen AN, Tortorelli DA, Sigmund O (2017) Combined shape and topology optimization for minimization of maximal von Mises stress. *Struct Multidiscip Optim* 55(5):1541–1557
- Love AEH (1892) A treatise on the mathematical theory of elasticity, Vol 1. Cambridge University Press, Cambridge
- Malvern LE (1969) Introduction to the mechanics of a continuous medium. Prentice-Hall
- Navarrina F, Muiños I, Colominas I, Casteleiro M (2005) Topology optimization of structures: a minimum weight approach with stress constraints. *Adv Eng Softw* 36(9):599–606
- Nocedal J, Wright SJ (2006) Numerical optimization, 2nd ed. Springer, Berlin
- Paris J, Navarrina F, Colominas I, Casteleiro M (2009) Topology optimization of continuum structures with local and global stress constraints. *Struct Multidiscip Optim* 39(4):419–437
- Paris J, Navarrina F, Colominas I, Casteleiro M (2010) Block aggregation of stress constraints in topology optimization of structures. *Adv Eng Softw* 41(3):433–441
- Park YK (1995) Extensions of optimal layout design using the homogenization method. Ph.D thesis, University of Michigan, Ann Arbor
- Pereira JT, Fancello EA, Barcellos CS (2004) Topology optimization of continuum structures with material failure constraints. *Struct Multidiscip Optim* 26(1-2):50–66
- Petersson J (2001) On continuity of the design-to-state mappings for trusses with variable topology. *Int J Eng Sci* 39(10):1119–1141
- Rozvany GIN, Birker T (1994) On singular topologies in exact layout optimization. *Struct Optim* 8(4):228–235
- Rozvany GIN (2001) On design-dependent constraints and singular topologies. *Struct Multidiscip Optim* 21(2):164–172
- Sharma A, Maute K (2018) Stress-based topology optimization using spatial gradient stabilized XFEM. *Struct Multidiscip Optim* 57(1):17–38
- Sigmund O (2007) Morphology-based black and white filters for topology optimization. *Struct Multidiscip Optim* 33(4-5):401–424
- Sigmund O (2009) Manufacturing tolerant topology optimization. *Acta Mech Sinica* 25(2):227–239
- Stolpe M, Svanberg K (2001) On the trajectories of the epsilon-relaxation approach for stress-constrained truss topology optimization. *Struct Multidiscip Optim* 21(2):140–151
- Svanberg K (1987) The method of moving asymptotes—a new method for structural optimization. *Int J Numer Methods Eng* 24(2):359–373
- Sved G, Ginos Z (1968) Structural optimization under multiple loading. *Int J Mech Sci* 10(10):803–805
- Talischi C, Paulino GH, Pereira A, Menezes IFM (2012a) PolyMesher: a general-purpose mesh generator for polygonal elements written in Matlab. *Struct Multidiscip Optim* 45(3):309–328
- Talischi C, Paulino GH, Pereira A, Menezes IFM (2012b) PolyTop: a Matlab implementation of a general topology optimization framework using unstructured polygonal finite element meshes. *Struct Multidiscip Optim* 45(3):329–357
- Talischi C, Paulino GH (2013) An operator splitting algorithm for Tikhonov-regularized topology optimization. *Comput Methods Appl Mech Eng* 253:599–608
- Timoshenko S, Goodier JN (1951) Theory of elasticity, 2 ed. McGraw-Hill
- Verbart A, Langelaar M, van Keulen F (2016) Damage approach: a new method for topology optimization with local stress constraints. *Struct Multidiscip Optim* 53(5):1081–1098
- Verbart A, Langelaar M, Keulen F v. (2017) A unified aggregation and relaxation approach for stress-constrained topology optimization. *Struct Multidiscip Optim* 55(2):663–679
- Wang MY, Wang S (2005) Bilateral filtering for structural topology optimization. *Int J Numer Methods Eng* 63(13):1911–1938
- Wang F, Lazarov BS, Sigmund O (2011) On projection methods, convergence and robust formulations in topology optimization. *Struct Multidiscip Optim* 43(6):767–784
- Wong KV, Hernandez A (2012) A review of additive manufacturing. *ISRN Mechanical Engineering* 2012, pp 1–10
- Xia Q, Shi T, Liu S, Wang MY (2012) A level set solution to the stress-based structural shape and topology optimization. *Comput Struct* 90:55–64
- Xu S, Cai Y, Cheng G (2010) Volume preserving nonlinear density filter based on Heaviside functions. *Struct Multidiscip Optim* 41(4):495–505
- Yang RJ, Chen CJ (1996) Stress-based topology optimization. *Struct Optim* 12(2):98–105
- Zegard T, Paulino GH (2016) Bridging topology optimization and additive manufacturing. *Struct Multidiscip Optim* 53(1):175–192

**Publisher's note** Springer Nature remains neutral with regard to jurisdictional claims in published maps and institutional affiliations.